Unrestricted Skyrme-tensor time-dependent Hartree-Fock model and its application to the nuclear response from spherical to triaxial nuclei

S. Fracasso,[*] E. B. Suckling, and P. D. Stevenson

Department of Physics, University of Surrey, Guildford, Surrey GU2 7XH, United Kingdom

(Received 29 May 2012; published 1 October 2012)

The nuclear time-dependent Hartree-Fock model formulated in three-dimensional space, based on the full standard Skyrme energy density functional complemented with the tensor force, is presented. Full self-consistency is achieved by the model. The application to the isovector giant dipole resonance is discussed in the linear limit, ranging from spherical nuclei (^{16}O and ^{120}Sn) to systems displaying axial or triaxial deformation (^{24}Mg, ^{28}Si, ^{178}Os, ^{190}W and ^{238}U). Particular attention is paid to the spin-dependent terms from the central sector of the functional, recently included together with the tensor. They turn out to be capable of producing a qualitative change on the strength distribution in this channel. The effect on the deformation properties is also discussed. The quantitative effects on the linear response are small and, overall, the giant dipole energy remains unaffected. Calculations are compared to predictions from the (quasi)-particle random-phase approximation and experimental data where available, finding good agreement.

I. INTRODUCTION

This work presents the full implementation of the Skyrme energy density functional (EDF) in time-dependent Hartree-Fock (TDHF) [1], including the tensor terms. The TDHF equations have been formulated on a three dimensional (3D) Cartesian grid with no spatial symmetry restrictions and include all time-odd terms. Consequently, it is possible to study different phenomena in both intrinsically spherical and deformed systems, in particular triaxiality, within the same formalism and without neglecting terms in the particle-hole (p-h) channel of the nuclear (and Coulomb) interaction. They can range from nuclear structure features like giant resonances (including nonlinearities and decay by particle emission) and large amplitude dynamics like collisions of nuclei (including fusion and fission processes). In this paper we focus on the first application, while another one about nucleus-nucleus collisions [2] will follow as an extension of recent related work [3,4].

The tensor force included in the original description of the Skyrme interaction [5] had mostly been omitted from Hartree-Fock calculations after initial explorations [6]. It has been the object of considerable interest in the past few years, when particular effort has been spent to attest the real limits of the mean-field approach. For a review of the "new generation" of tensor studies we refer to Ref. [7], the authors of which extensively analyzed the performance of several Skyrme-tensor functionals on ground-state properties of spherical systems. In such cases, only the so-called time-even terms of the EDF, built on densities which maintain the same sign under the time-reversal operation, contribute. Their coupling constants are typically fixed through a selection of experimental and empirical data.

A situation similar to the spherical case, although not identical, occurs in axially deformed nuclei. The full spatial

rotational invariance is lost in the intrinsic system of reference, giving rise to extra contributions to the one-body potential with respect to the spherical case [8]; however, one expects the parity and the total angular-momentum projection along the symmetry axis are still good quantum numbers, the time-reversal invariance is preserved, and all the time-odd terms of the functional vanish in the ground-state. This fact is maintained when pairing effects are introduced, as long as the particle-particle scattering involves pairs in time-reversal states. In Ref. [9], the performance of time-even tensor terms fixed on spherical systems [7] was studied against deformed ground-state properties. Fewer analyses are available for triaxial ground-states (cf. Refs. [10,11] and references therein), where the spatial symmetry properties are further broken, but the time-reversal invariance is known to be still preserved.

Increasing the complexity of the problem, a different situation occurs in odd-A and odd-odd nuclei and, in general, in the presence of cranking, when the time-reversal invariance is broken and the Kramer's degeneracy is removed [12–14]. In such situations, in fact, time-odd terms become active. The effects from the time-odd terms that originate from the Skyrme central and spin-orbit force have been studied through their influence on rotational bands of superdeformed nuclei [15]. More recently, the full Skyrme time-odd sector, including the tensor terms, has been taken into account, too [16].

Regarding vibrational states, on the side of the (nonrelativistic) self-consistent random-phase approximation (RPA), which does not model the pairing correlations and which corresponds to the small amplitude (linear) limit of TDHF, progress has been obtained by including the residual Skyrme-tensor interaction in formulations on a spherical p-h configuration basis. As known, the time-odd terms play an essential role in explaining the nuclear response in some cases. Calculations including the tensor in both some "neutral" [17] and charge-exchange channels [18] have been published. Similarly to previous work, the relative contribution of the residual two-body versus the underlying mean-field tensor effects was

---
[*]s.fracasso@surrey.ac.uk

discussed by these authors, but no further considerations on the various functional's terms and their interplay were made. Skyrme-tensor RPA calculations in infinite matter [19] have been performed as well.

No self-consistent implementation of the Skyrme functional complemented by the tensor interaction in a deformed (quasi-)particle random-phase approximation [(Q)RPA] is currently available. Our task with the more general TDHF approach is also aimed at filling this gap, allowing more applications on the same footing. In this TDHF model all the Skyrme-tensor EDF terms have been derived and implemented; the specific role played by some of them, where the focus is on spin-dependent terms that were previously neglected, will be outlined and issues related to self-consistency discussed. Although the comparison between TDHF and RPA approaches is not the aim of this paper and more can be found elsewhere, in Sec. II A 1 we will recall some (standard) terminology and elements useful to follow the discussion.

Previous applications of TDHF to zero-temperature giant resonances, including time-odd terms from modern Skyrme EDFs and exploiting computational power which was not available in the past, exist. In Ref. [20], the linear response in some light spherical and deformed nuclei was studied by comparing different approaches (TDHF with absorbing boundary conditions and continuum RPA formulated with the Green's functions formalism); the terms depending on the square of the momentum density (j^2), which affects the effective mass, and on the square of the spin density (S^2) were discussed, while other spin-dependent terms were omitted from those calculations. The authors of Ref. [21] pointed out the relevance of the Skyrme time-odd spin-orbit in suppressing spurious spin excitations in free translational motion, associated to a nonphysical energy dissipation in heavy-ion collisions. This was explained as a consequence of the Galilean invariance restoration when the spin-orbit sector of the functional is fully included.

After the formalism is introduced (Sec. II), we present (Sec. III) the results about the isovector dipole response (IVD) for some representative cases. It is well known that most of the IVD transition strength is concentrated in the giant dipole resonance (IVGDR or simply GDR), the first collective nuclear excitation that was discovered [22–24]. Although the major effect from the inclusion of the spin-dependent terms is not expected in this case, we focus on it according to the tradition of the TDHF calculations, as this is the simplest, experimentally well known, nonspherical excitation that can be reproduced. Many theoretical simulations are available, ranging from more phenomenologic approaches (where the important dependence on external input can produce accurate calculations but drastically limits the predictive power), down to microscopic descriptions with no *ad hoc* adjustable parameters, to which group our model belongs.

In Sec. IV conclusions will be summarized. The derivation of the tensor contribution to the Skyrme EDF is provided in Appendix A as an extension of Ref. [25], where the functional form of the energy density from the central and spin-orbit part of the force was written without assuming a time-reversal invariant system. Finally, the expressions and possible implementations of the densities and currents of the functional have been added in Appendix B.

II. FORMALISM

The first part of this section recalls the basic features of the TDHF theory and the numerics adopted in this work, while the second one focuses on the full Skyrme-tensor energy density functional, implemented in TDHF with no symmetry restrictions. Some of the performed verification and validation tests will be discussed.

A. Time-dependent Hartree-Fock model

As mentioned in the Introduction, the theoretical framework chosen to implement the unrestricted Skyrme energy density functional, to which the following section is dedicated, is the 3D Cartesian time-dependent Hartree-Fock. In this theory [26], with semiclassic limit given by the Vlasov equation, well known in plasma physics and astrophysics, the interaction among particles is modelled in terms of the interaction with the one-body potential, which, after (or under) the action of an external field, changes in time through the dependence on the density itself. The master expression of the theory derives from the von Neumann equation, the quantum-mechanical version of the classical Liouville equation which provides the time evolution of the A-body density matrix. Through the constraint $\hat{\rho}_A^2 = \hat{\rho}_A$ for the full density matrix, the system can be represented by a pure state solution of the associated Schroedinger equation. In TDHF, the previous relation is assumed to hold for the one-body density matrix $\hat{\rho}_1$ (hereafter $\hat{\rho}$), so that the A-particle wave function can be represented by a Slater determinant at any time (the backward relation holds, too; details can be found in Ref. [27]). As a matter of fact, the von Neumann equation, which gives rise to the BBGKY hierarchy for the reduced one-body, two-body, etc., densities, now simplifies to a one-body problem

$$i\hbar\delta_t\hat{\rho} = [\hat{h}, \hat{\rho}], \tag{1}$$

which can be equivalently represented by the (nonlinear) set of one-body equations

$$i\hbar\delta_t\psi^{(i)}(\mathbf{x}, t) = \hat{h}[\rho(t)]\psi^{(i)}(\mathbf{x}, t), \tag{2}$$

one for each spinor $\psi^{(i)}(\mathbf{x}, t) = \sum_{\omega=2m_s} \phi^{(i)}(\mathbf{x}, \omega, t)\xi(\omega)$ identified by the index i ($\omega = 2m_s = \pm 1$), with initial conditions given further on (the dependence of the one-body Hamiltonian on the particle density can be generalized). A time-dependent external field can be inserted in the previous equation (2). In this work, it will be assumed to simply act as a δ function in time, used to prepare the initial conditions for the time evolution. The external field acting on the system can be defined, in particular, as a one-body operator able to induce an isovector response (protons and neutrons move in opposition of phase) with no charge mixing, that is, in the form

$$\hat{F} = \sum_{rs} \langle s|F|r\rangle a_r^\dagger a_s, \tag{3}$$

where a_r^+ and a_s are creation and annihilation operators in the HF basis and $F = \sum_i Df(\boldsymbol{x}_i, \omega_i)\tau_z(i)$. This external field transfers energy (regulated by the strength D) and a selection of angular momentum to the nucleus, causing a displacement of the proton and neutron centers of mass, compatible deformation and/or spin fluctuations; in such a way, the system is set in oscillation with all the possible frequencies. In other words, after the external action, the A-particle wave function is no longer an eigenstate of the static ("unperturbed") Hamiltonian and starts to evolve in time. In a microscopic picture, the external kick induces p-h transitions that are allowed by the selection rules, so, at time $t = 0$, each Hartree Fock eigenstate $\phi_i^{(0)}$ is transformed into a wave packet,

$$\psi^{(i)}(\boldsymbol{x}, t = 0) = e^{i\hat{F}}\phi_i^{(0)}(\boldsymbol{x}) = \sum_l \alpha_{il}\phi_l^{(0)}(\boldsymbol{x}), \qquad (4)$$

where the index l spans the full HF spectrum. The label (i) at the left-hand side of the previous equation simply enumerates the wave functions obtained by boosting the HF solution having a set of quantum numbers i. Using (4) as initial condition, where only the choice of the external operator $\hat{F}$ is arbitrary and (partly) defines the problem under study, the equations (2) are solved and a new set of quasiparticles $\{\psi^{(i)}(\boldsymbol{x}, t)\}$ is given at any time. Clearly, under the action of the one-body potential, mixings other than those initially generated by $\hat{F}$ are produced.

In practical implementations, according to long-standing prescriptions [28], the time is discretized and the evolution operator is implemented in a Taylor expansion. The time step size and the order at which the expansion is arrested are two mutually dependent parameters chosen in order to ensure the total energy and norms are conserved in the "dynamics" within acceptable accuracy.

The system response is analyzed by following the time evolution of the expectation value for the one-body operator of interest,

$$\langle\hat{O}\rangle(t) = \langle\Phi_t|\hat{O}|\Phi_t\rangle \qquad (5)$$

(referred to the ground-state value). One can replace the A-particle Slater determinant at time t (Φ_t) by the simple product of the involved TDHF wave functions and recast the previous equation as

$$\langle\hat{O}\rangle(t) = \sum_i \langle\psi^{(i)}(\boldsymbol{x}, t)|O(\boldsymbol{x})|\psi^{(i)}(\boldsymbol{x}, t)\rangle, \qquad (6)$$

which can be conveniently expressed in terms of properly defined one-body densities. For example, the well-known (effective) isovector dipole response along the λ direction is based on the expectation values

$$\langle\hat{O}_{1^-01}^K\rangle(t) = \frac{\tilde{D}}{A}\int \lambda[Z\rho_n(\boldsymbol{x}, t) - N\rho_p(\boldsymbol{x}, t)]d\boldsymbol{x}, \qquad (7)$$

depending on the time-dependent isovector density $\rho_{10}(\boldsymbol{x}, t) = \rho_n(\boldsymbol{x}, t) - \rho_p(\boldsymbol{x}, t)$. It is associated to the choice

$$f_{1K}(\boldsymbol{x}, \omega) = \mathcal{Y}_{1K}(\boldsymbol{x})|\boldsymbol{x}|I_\sigma \qquad (8)$$

for $f(\boldsymbol{x}, \omega)$, where I_σ is the identity operator in the spin space (kept implicit in what follows) and $\{\mathcal{Y}_{1K}\}_{K=-1,0,1} = \{\sqrt{\frac{3}{4\pi}}\frac{\lambda}{|\boldsymbol{x}|}\}_{\lambda=x,y,z}$ is the set of $l = 1$ real spherical harmonics written in Cartesian coordinates ($\tilde{D} = D\sqrt{\frac{3}{4\pi}}$, $e = 1$). The subscript in Eq. (7) denotes the $J^\pi ST$ quantum numbers. The signal obtained on top of a spherical ground-state is clearly invariant under any rotation in space of the boost direction. The center-of-mass correction in the definition of the operator is included in order to remove the translational zero mode from the strength function (the boost needs proper weights as well).

Under the hypothesis $\hat{O} = \hat{F}$, it is possible to show that the transition strength distribution associated to $\hat{O}$

$$S_{\hat{O}}(E) = \sum_\nu |\langle\nu|\hat{O}|-\rangle|^2\delta(E - E_\nu), \qquad (9)$$

where ν labels the excited states in the small amplitude limit and $|-\rangle$ is the HF vacuum, can be obtained through

$$S_{\hat{O}}(E) = -\frac{1}{\pi}\frac{\mathcal{F}[\langle\hat{O}\rangle(t)]}{\mathcal{F}[Dg(t)]}, \qquad (10)$$

where $\mathcal{F}$ denotes the Fourier transform operation and $g(t)$ is the generalization of the (factorized) time profile of the external operator. The proof of the equivalence between Eqs. (9) and (10) can be found in Refs. [29,30] (the rearrangement arising from density-dependent Hamiltonian terms is usually considered negligible).

The presence of the factor D in the denominator of Eq. (10) guarantees that the response is kept constant for different boost strength in the small-amplitude (RPA) regime. This rescaling can be used as an indicator to test the validity of the assumption of linearity. In fact, when the boost amplitude is increased above a certain threshold, the channel for nonharmonic effects, which, under a one-body view, accounts for 3p-1h (3h-1p) vertices [31], is opened.

Choices differing from $\hat{O} = \hat{F}$ allow one to select the signal of interest, like a specific multipole or spin (isospin) component, among the various response channels which can be opened by a given external operator and mixed up during the dynamic evolution. For example, the 1^- states are a mixture of both non-spin-flip ($S = 0$, $S = 1$) and spin-flip ($S = 1$) components, that is, in the microscopic picture of the RPA, nucleons can also reverse the spin when undergoing particle-hole transitions. A large fraction of the isovector $S = 1$ dipole strength is collected in the giant spin-dipole resonance (IVSDR or, hereafter, SDR). Several investigations on both the experimental and the theoretical side (see Ref. [32] and references therein) have been dedicated to the problem of the GDR-SDR splitting, which markedly reflects the dependence of the effective interaction on the incident energy. A schematic model predicts the SDR to be lower in energy than the GDR, on the basis of a residual interaction being slightly less repulsive in the spin-isospin ($S = 1$, $T = 1$) channel than in the isospin ($S = 0$, $T = 1$) one [33]. From general arguments, in a limit case one can find a highly collective 1^- state exhausting the whole sum rule for the dipole (or for the spin-dipole) operator, so that zero transition probability associated to the other one is left [34]. In practice, this is less likely to occur, the two resonances overlap, and 1^- states displaying non vanishing

transition strength associated to either of the operators can be found to be degenerate or lying close in energy (see the examples in Ref. [35]).

As giant resonances are above threshold, particle emission is expected and it can be modelled in TDHF [36]. A discussion about the lifetime of the TDHF wave functions can be found, e.g., in Ref. [37], where a comparison between the performance of TDHF and the continuum-RPA in the matter of escaping widths and the possibility of comparing to experimental information was discussed.

Reference [38] presented the effect of two-body correlations on the mass dispersion from giant resonances, incorporated in the standard TDHF as fluctuation of the one-body observable of interest on the basis of the Balian-Vénéroni approach [39], which turned out to be important. As a matter of fact, although TDHF takes into account the coupling to the continuum and those anharmonicities that can be captured through one-body operators, extensions are required to fully describe the spreading width of the resonances. Effort has been devoted to formulate extensions of TDHF which go beyond the mean-field approximation, capable of modeling coherent collisional terms as well as incoherent effects, like those leading to 2p-2h admixtures into the strength function from nondiagonal couplings to low-lying phonons or noncollective 1p-1h bubbles [40]. We recall that couplings of 1p-1h to high-lying 2p-2h states in spin-isospin channels are expected to be favored by the tensor, a mechanism which, spreading strength towards high energies, has been invoked to fully explain the quenching of the Gamow-Teller (GTR) and the SDR (see Ref. [33]), collective states of particular interest for astrophysical processes and particle physics.

If the standard TDHF approach and the extensions recalled just above describe a single path in the time domain, stochastic formulations of the theory are available, which were shown to be closely related to the Boltzmann-Langevin equation (cf. Refs. [41,42] and references therein; cf. also the discussion in Ref. [43]).

1. Comments on TDHF and RPA models

This section is not aimed at providing a complete review of similarities and differences between the two approaches, their various formulations, or the physics involved. Instead, some (standard) terminology is recalled, together with a few elements useful to better follow the discussion. Besides the fact that TDHF is a more general theory than the RPA, it is useful to remark on some technical differences when the former is employed in the linear limit.

The RPA framework, first formulated for plasma physics in 1953 [44], involves, besides the construction of the static mean-field, the computation of the two-body matrix elements of the residual interaction in the p-h channel. In the most microscopic approaches, which make little use of *ad hoc* adjustable parameters, they are respectively defined as the first and second derivative of the energy density functional (given by *ansatz* or built on an effective interaction like Skyrme) with respect to the particle density fluctuation [45]. The derivation must be performed from the most general expression of the

energy density, that is, built without the symmetry restrictions allowed in special cases (cf. Refs. [25,46]; see also Ref. [2]). As a matter of fact, not only are ground-state spin saturation properties [which here means $\sum \psi_i^*(\bm{x})\bm{\sigma}_i\psi_i(\bm{x}) = 0$] and spatial symmetries usually broken when exciting the system, but also, in some cases, the excitation is mostly driven by terms that vanish in the Hartree-Fock approximation.

Self-consistency, as intended in the sense of the RPA (we will not discuss the case of the various types of separable RPAs; information can be found in Ref. [47]) means that EDF contributions are not dropped when proceeding from the Hartree-Fock mean-field to the computation of excited states. Under this condition, provided the model space is complete, it is commonly known that symmetries spontaneously broken by the Hartree-Fock approximation are automatically restored and spurious modes, within the limits of numerical accuracies, become orthogonal to the physical spectrum and degenerate with the ground-state (zero modes) [48].

Concerning the TDHF model, a full discussion about the symmetry breaking should be provided, which is beyond the scope of this work. We only add that, as for the RPA approaches, numerical inaccuracies can produce spurious mixings and alter the strength distribution. However, a lack of "consistency" can be produced also in other ways, for example, from an incomplete implementation of the functional at the mean-field level with respect to the procedure adopted when fitting its parameters, as well as any use which produces lack or overcounting of effects.

Regarding an effective two-body force with no density-dependent coupling constants, as for the tensor terms by Skyrme, one can avoid working out the energy density in order to derive the mean-field and the two-body residual interaction, because, in the absence of rearrangement, the latter would be identical to the starting force. However, one would miss, in this case, the link of the interaction terms back to the corresponding energy functional contribution, which one usually refers to when comparing different calculations. Although it is recognized that the globally fitted values of the Skyrme parameters should be interpreted by looking at the functional as a whole, it is still interesting to study the role of the various terms by setting some coupling constants to zero or by artificially modifying the functional in other ways. If the consistency breakings produced in such way are not dramatic, this operation can reveal general features of the effective interaction and point to drawbacks and merits of one specific parametrization. With such an aim, the use of Skyrme-like EDFs, that is, non-two-body interaction based EDFs, more or less rich in density-dependent coupling constants and derivatives, has become quite widely investigated.

In the standard TDHF theory, only the mean-field operator is required in both the static (HF ground-state) and dynamic (residual effects) calculations. The implementation of the functional is, in this sense, much less involved with respect to the RPA approach and the fulfillment of self-consistency is less demanding, especially in comparison to RPAs formulated in the coordinate space. Clearly, the effects corresponding to the various terms, coupled one another through the densities, are not expected to be simply additive. It occurs in analogy to RPA

whenever a different matrix is diagonalized once two-body contributions are dropped.

Concerning the microscopic understanding of the results, in the widely employed RPA models formulated in the configuration space, the equation of motion is reduced to the diagonalization of a matrix built on a p-h basis; the solution immediately provides the microscopic structure of the excited states in terms of the simplest excitations assumed within the theory and this repays the effort of building the two-body matrix elements. The RPA transition strength distribution is built up by a linear combination of the one-body p-h transition amplitudes (OBTAs) for the given operator, with weight depending on the expansion coefficients resulting from the diagonalization (which reduce to 0 or 1 in the noninteracting limit, corresponding to the "unperturbed" response) and interference is properly accounted for. These ingredients provide together a useful guideline to microscopically interpret the RPA response (at least in a weak-coupling regime). One can understand, for example, which p-h wave function contributes more strongly (in terms of OBTA and relative weight) to an eigenstate displaying a relevant amount of transition probability for the operator of interest. Moreover, one can attest to what extent the degree of mixing among the p-h states, the mechanism underpinning the collectivity, where the relative importance between the strength of the residual interaction and the unperturbed energies plays a key role, is mainly due to one or the other term of the force. The reader can refer to one example in Ref. [49], which shows how the residual Skyrme spin-orbit is able to admix extra p-h configurations with opposite spins in the considered low-lying RPA state.

Although less commonly studied, and also considering some interpretation issues, microscopic information can be extracted from TDHF simulations as well, provided the requested operations are built in. Examples of microscopic analyses of TDHF calculations can be found in Refs. [50,51]. Further considerations of this topic are deferred to the future.

B. Unrestricted Skyrme energy density functional

TDHF is a well-established implementation of the density functional approach in nuclear physics [8]. The starting point is the static (effective) Hartree-Fock energy density $\mathcal{H}(\boldsymbol{x})$

$$E_{\text{HF}} = \langle -|\hat{H}|-\rangle_{\text{as}} = \int \mathcal{H}(\boldsymbol{x}) d\boldsymbol{x}, \qquad (11)$$

from which the mean-field can be derived. In our case, in the previous equation $\hat{H}$ is the effective Skyrme Hamiltonian and $|-\rangle$ is the Hartree-Fock ground-state. In general, a nonlocal energy density can be defined. Due to the effective nature of the nuclear Hamiltonian and the associated mean-field, the Hartree-Fock (Hartree-like) equations share the same philosophy of the electronic Kohn-Sham equations [52].

Although the Skyrme interaction is constructed as a contact force, a fact that allows the implementation of the functional in terms of one-body densities depending on a single point of space, finite-range effects are simulated through the derivatives of the wave functions. In fact, the standard Skyrme-tensor HF energy density is expressed like a sum of terms bilinear in the

particle or spin densities

$$\rho(\boldsymbol{x}) = \rho(\boldsymbol{x}, \boldsymbol{x}')\big|_{\boldsymbol{x}=\boldsymbol{x}'} = \sum_i \sum_\omega \phi_i^*(\boldsymbol{x}', \omega)\phi_i(\boldsymbol{x}, \omega)\bigg|_{\boldsymbol{x}=\boldsymbol{x}'} \qquad (12)$$

$$\boldsymbol{S}(\boldsymbol{x}) = \boldsymbol{S}(\boldsymbol{x}, \boldsymbol{x}')\big|_{\boldsymbol{x}=\boldsymbol{x}'}$$

$$= \sum_i \sum_{\omega,\omega'} \phi_i^*(\boldsymbol{x}', \omega')\phi_i(\boldsymbol{x}, \omega)\langle\omega'|\boldsymbol{\sigma}|\omega\rangle\bigg|_{\boldsymbol{x}=\boldsymbol{x}'}, \qquad (13)$$

and other kinds of densities defined by the up-to-second-order derivation of these objects, before the local limit is taken (see Ref. [53] for higher order EDFs). In the equations above, the spin components of the spinor i are represented by $|\omega\rangle$ [previously indicated by $\xi(\omega)$] and $\boldsymbol{\sigma}$ are the Pauli matrices. Once the static densities are replaced by those built on the solutions of the time-dependent one-body equations, the total energy density gains a time dependence $[\mathcal{H}(\boldsymbol{x}) \to \mathcal{H}(\boldsymbol{x}, t)]$, although its functional form remains unchanged with respect to the static case.

When only the central and spin-orbit terms of the Skyrme force are retained, not all the combinations allowed by the symmetries, among those depending on the second-order derivatives, appear in the corresponding functional. The tensor force provides a richer structure, introducing, in the N-N interaction, the dependence on the relative spin orientation according to

$$v_\tau(1, 2) = V_{1,2}^\tau(\boldsymbol{r}) = 4V_{1,2}^\tau(r)\left[3\frac{(\boldsymbol{\sigma}_1 \cdot \boldsymbol{r})(\boldsymbol{\sigma}_2 \cdot \boldsymbol{r})}{r^2} - \boldsymbol{\sigma}_1 \cdot \boldsymbol{\sigma}_2\right], \qquad (14)$$

where $\boldsymbol{r}$ is the relative position of the two interacting particles and $V_{12}^\tau(r)$ is the spatial form factor that also accounts for the isospin dependence. It is the only (local) force able to explain the deuteron quadrupole moment, being able to transfer to a two-particle wave function up to two units of orbital angular momentum and active only between spin triplet states. As a one-body potential, the tensor force is able to mix single-particle states that differ by one or two units of orbital angular momentum, possibly introducing a parity mixing.

Within a meson exchange model, the form factor of Eq. (14) is modelled as a Yukawa potential and its zero-range limit can be parametrized in the Skyrme form

$$\begin{aligned}
v_\tau(1, 2) = {} & \frac{T}{2}[(\boldsymbol{\sigma}_1 \cdot \boldsymbol{k}')(\boldsymbol{\sigma}_2 \cdot \boldsymbol{k}')\delta + \delta(\boldsymbol{\sigma}_1 \cdot \boldsymbol{k})(\boldsymbol{\sigma}_2 \cdot \boldsymbol{k})] \\
& - \frac{T}{6}(\boldsymbol{\sigma}_1 \cdot \boldsymbol{\sigma}_2)[k'^2\delta + \delta k^2] \\
& + \frac{U}{2}[(\boldsymbol{\sigma}_1 \cdot \boldsymbol{k}')\delta(\boldsymbol{\sigma}_2 \cdot \boldsymbol{k}) + (\boldsymbol{\sigma}_1 \cdot \boldsymbol{k})\delta(\boldsymbol{\sigma}_2 \cdot \boldsymbol{k}')] \\
& - \frac{U}{6}(\boldsymbol{\sigma}_1 \cdot \boldsymbol{\sigma}_2)[\boldsymbol{k} \cdot \delta\boldsymbol{k} + \boldsymbol{k}'\delta \cdot \boldsymbol{k}], \qquad (15)
\end{aligned}$$

where δ denotes $\delta(\boldsymbol{x}_1 - \boldsymbol{x}_2)$ and, as usual, $\boldsymbol{k} = \frac{1}{2i}(\boldsymbol{\nabla}_1 - \boldsymbol{\nabla}_2)$ and $\boldsymbol{k}' = -\frac{1}{2i}(\boldsymbol{\nabla}_1' - \boldsymbol{\nabla}_2')$ respectively act on the right and on the left. This fully invariant interaction term corresponds to the original one [5] and provides the same identical contribution to the Hartree-Fock energy density (Appendix A) as the more compact expression often employed in literature (cf. Ref. [6]

and more recent works). By using basic angular-momentum algebra, the previous equation can be recast in terms of products of tensors of rank 2 in spin and momentum (see, e.g., Ref. [17]).

Although the tensor force is able to act between relative $L = 2$ states, where the centrifugal barrier keeps the nucleons apart, so the long-range attractive part of the N-N interaction ($r > 3$ fm) is probed, there is currently no evidence that an intra-medium finite-range tensor force performs better than a contact, velocity-dependent, parametrization. Some remarks

about the quality of the zero-range approximation for the tensor force were proposed by the authors of Ref. [54]. Recent comparisons between Skyrme (SLy5 + t of Ref. [55]) and, in particular, the GT2 Gogny force of Ref. [56] can be found in Ref. [57]. Not many finite-range effective forces complemented with the tensor are available and further studies are envisaged for the future.

In the proton-neutron formalism, the contribution to the energy density associated to the tensor force (15), once the exchange is taken into account, reads

$$
\begin{aligned}
\mathcal{H}_{\text{tens}}(x) ={}& 2B_{\nabla S}\nabla \cdot S_n(x)\nabla \cdot S_p(x) + A_{\nabla S}\sum_q (\nabla \cdot S_q(x))^2 + 2B_{J_0}J_n^0(x)J_p^0(x) + A_{J_0}\sum_q \left(J_q^0(x)\right)^2 \\
&+ 2B_{J_1}\boldsymbol{J}_n(x) \cdot \boldsymbol{J}_p(x) + A_{J_1}\sum_q (\boldsymbol{J}_q(x))^2 + 2B_{J_2}\underline{J}_n(x)\underline{J}_p(x) + A_{J_2}\sum_q (\underline{J}_q(x))^2 \\
&+ B_F[S_n(x) \cdot F_p(x) + S_p(x) \cdot F_n(x)] + A_F\sum_q S_q(x) \cdot F_q(x) + B_G[S_n(x) \cdot G_p(x) + S_p(x) \cdot G_n(x)] \\
&+ A_G\sum_q S_q(x) \cdot G_q(x) + B_T[S_n(x) \cdot T_p(x) + S_p(x) \cdot T_n(x)] + A_T\sum_q S_q(x) \cdot T_q(x) \\
&+ B_{\Delta S}[S_n(x) \cdot \Delta S_p(x) + S_p(x) \cdot \Delta S_n(x)] + A_{\Delta S}\sum_q S_q(x) \cdot \Delta S_q(x).
\end{aligned}
\tag{16}
$$

For a generic term α of the functional, the A_α and B_α coupling constants enter the expression of the proton or neutron mean-field, respectively felt by a particle with the same and opposite isospin. In terms of the commonly employed isoscalar and isovector coefficients C_T^α, they satisfy the relations $A_\alpha = C_0^\alpha + C_1^\alpha$ and $B_\alpha = C_0^\alpha - C_1^\alpha$. The C_T^α coupling constants are related to the Skyrme parameters as tabulated in Ref. [58], according to the convention for the EDF explained below.

The most evident difference with respect to the standard Skyrme functional, based only on the central and spin-orbit terms of the force, is the presence of two pseudovector densities built on the tensor product of the nabla operators,

$$
F(x) = \tfrac{1}{2}\{[(\nabla' \otimes \nabla) + (\nabla \otimes \nabla')]S(x, x')\}_{x=x'}, \tag{17}
$$

$$
G(x) = \tfrac{1}{2}\{[(\nabla' \otimes \nabla') + (\nabla \otimes \nabla)]S(x, x')\}_{x=x'}, \tag{18}
$$

where $F_\mu = \tfrac{1}{2}\sum_\nu[(\nabla' \otimes \nabla) + (\nabla \otimes \nabla')]_{\mu\nu}S_\nu$ and $\otimes$ denotes the usual tensor product between vectors $(A \otimes B)_{\mu\nu} = A_\mu B_\nu$. The $S \cdot F$ and $S \cdot G$ terms are connected through the $(\nabla \cdot S)^2$ term according to the equation

$$
[F(x) + G(x)] \cdot S(x) = -\tfrac{1}{2}[\nabla \cdot S(x)]^2, \tag{19}
$$

which applies when integration is assumed. The previous relation can be used to successfully switch from Eq. (16) to the formulation of the EDF of Ref. [58], where the G density was not defined and only the $S \cdot F$ terms appear, with proper weights. In this paper we will work with the formulation based on the choice $C_T^G = 0$, too. More details can be found in Appendix A, where the derivation of Eq. (16) is provided. Indeed, since the terms of the functional are not independent

of each other, for example, the relation [59]

$$
[\nabla \cdot S(x)]^2 = -S(x) \cdot \Delta S(x) - [\nabla \times S(x)]^2 \tag{20}
$$

also holds, many equivalent formulations for the energy density can be worked out.

The $S \cdot F$ and $S \cdot G$ terms contribute to maintain the Galilean invariant properties of the standard Skyrme functional when the tensor is made active. In particular, they are related to the pseudoscalar, vector, and pseudotensor densities J_0, J, $\underline{J}$ and the pseudovector spin kinetic density T. The latter is defined by

$$
T(x) = [\nabla \cdot \nabla' S(x, x')]_{x=x'}, \tag{21}
$$

where a generic component T_μ depends on $\nabla \cdot \nabla' S_\mu$. The former three objects are those that represent the trace, the antisymmetric, and the symmetric parts [7] of the pseudotensor spin current

$$
\overleftrightarrow{J}(x) = \frac{1}{2i}[(\nabla - \nabla') \otimes S(x, x')]_{x=x'}, \tag{22}
$$

which decomposes into

$$
J_{\mu\nu} = \frac{1}{3}\delta_{\mu\nu}J_0 + \frac{1}{2}\sum_{i=x,y,z}\epsilon_{i\mu\nu}J_i + \underline{J}_{\mu\nu}, \tag{23}
$$

with $\epsilon_{i\mu\nu}$ being the Levi-Civita tensor; their square satisfies the relations

$$
J_0^2 = \sum_{\mu\nu} J_{\mu\mu}J_{\nu\nu}, \tag{24}
$$

$$
\boldsymbol{J}^2 = \sum_{\mu\nu} J_{\mu\nu}(J_{\mu\nu} - J_{\nu\mu}), \tag{25}
$$

$$
\underline{J}^2 = \frac{1}{2}\sum_{\mu\nu} J_{\mu\nu}(J_{\mu\nu} + J_{\nu\mu}) - \frac{1}{3}J_0^2 \tag{26}
$$

and simple algebra leads to

$$\overset{\leftrightarrow}{J}{}^2 = \tfrac{1}{3} J_0^2 + \tfrac{1}{2} \boldsymbol{J}^2 + \underline{J}^2; \tag{27}$$

the usual definition for the scalar product between tensors $\overset{\leftrightarrow}{A}\overset{\leftrightarrow}{B} = \sum_{\mu\nu} A_{\mu\nu} B_{\mu\nu}$ has been used. As long as triaxiality is absent, $J_0 = \mathrm{Tr}\,\overset{\leftrightarrow}{J}$ is zero (in the presence of subscripts, J_0 will be denoted by $J^{(0)}$). In spherical symmetric nuclei, the sum over μ, ν in Eq. (26) vanishes as well [2], so one recovers the reduction of $\overset{\leftrightarrow}{J}{}^2$ to $\tfrac{1}{2} \boldsymbol{J}^2$. The J_0, $\boldsymbol{J}$, and $\underline{J}$ densities enter the central sector of the standard Skyrme functional with weights that allow the replacement

$$C_T^{J_0,c} \big(J_T^{(0)}\big)^2 + C_T^{J_1,c} \boldsymbol{J}_T^2 + C_T^{J_2,c} \underline{J}_T^2 = C_T^{J,c}\, \overset{\leftrightarrow}{J}_T^2 \tag{28}$$

for $T = 0, 1$, since $C_T^{J,c} = 3C_T^{J_0,c} = 2C_T^{J_1,c} = C_T^{J_2,c}$ ($C_T^\alpha = C_T^{\alpha,c} + C_T^{\alpha,t}$, where c = central, t = tensor). Unless the tensor is switched on, the two implementations, in terms of $\overset{\leftrightarrow}{J}$ [25] or the formulation where J_0, $\boldsymbol{J}$, and $\underline{J}$ are kept separated [58], are interchangeable. In this case, the Galilean invariance only relates the spin-current terms to those depending on the spin kinetic density $\boldsymbol{T}$ ($C_T^{T,c} = -C_T^{J_2,c}$). When the tensor is introduced, the following relations among the parameters must hold for the Galilean invariance to be respected

$$3C_T^{J_0} + C_T^T + 2\big(C_T^F - C_T^G\big) = 0,$$
$$4C_T^{J_1} + 2C_T^T - \big(C_T^F - C_T^G\big) = 0, \tag{29}$$
$$2C_T^{J_2} + 2C_T^T + \big(C_T^F - C_T^G\big) = 0$$

and $3/10 C_T^{J_0,t} = -2/5 C_T^{J_1,t} = C_T^{J_2,t}$. This is realized for the Skyrme-tensor functional; in order to prove the invariance, it is useful to know that under the local gauge (Galilean) operation $T_G : \psi_i(\boldsymbol{x}) \rightarrow e^{i\boldsymbol{k}\boldsymbol{x}} \psi_i(\boldsymbol{x})$, the $\boldsymbol{F}$ and $\boldsymbol{G}$ densities transform according to

$$T_G(F_\mu(\boldsymbol{x})) = F_\mu(\boldsymbol{x}) + k_\mu \boldsymbol{k} \cdot \boldsymbol{S}(\boldsymbol{x}) + k_\mu J_0(\boldsymbol{x})$$
$$+ \sum_\nu k_\nu J_{\mu\nu}(\boldsymbol{x}), \tag{30}$$
$$T_G(G_\mu(\boldsymbol{x})) = G_\mu(\boldsymbol{x}) - k_\mu \boldsymbol{k} \cdot \boldsymbol{S}(\boldsymbol{x}) - k_\mu J_0(\boldsymbol{x})$$
$$- \sum_\nu k_\nu J_{\mu\nu}(\boldsymbol{x}). \tag{31}$$

In total, the Galilean invariance imposes constraints on 8 (6 without the tensor) of the 14 time-odd coupling constants of the whole Skyrme-tensor functional (in the isospin formalism and in the formulation where $C_T^G = 0$), which, in such a way, are determined from the corresponding even partners. We refer to Refs. [25] [notice the misprint in Eq. (4.6), where $\boldsymbol{k}^2$ has to be replaced by $\boldsymbol{k}^2 \rho(\boldsymbol{r})$] and [58] for the full set of relations concerning the Galilean invariance properties and we proceed with some other comments.

The inclusion of the spin-current $\overset{\leftrightarrow}{J}{}^2$ terms, which, as known, affect the spin-orbit splitting in the absence of spin saturation (here in the sense that each pair of spin-orbit partners is not fully filled up), is required in forces that took them into account during the fit. Neglecting them leads to a break of consistency in terms of an incomplete implementation of the functional. For a more complete discussion, refer to Ref. [60], where a comparison between predictions from the SLy4 force, fitted without that contribution ("type I" force), and the SLy5 set, which included it ("type II"), was considered; ambiguities related to the former type of force were pointed out. In particular, it was discussed that the contribution from the $\overset{\leftrightarrow}{J}{}^2$ terms in computing the excited states can be more important than in the ground-state, with the result that standard fitting procedures, unable to capture some physics through the ground-state observables, can lead to poor results when computing collective excitations. For this reason, suppressing those terms from the residual interaction of "type I" forces can lead to an error larger than a RPA self-consistency breaking approach, although (unwanted) case-by-case considerations with such parametrizations might be required.

It similarly holds for the time-odd sector of the functional. The central $\boldsymbol{S} \cdot \boldsymbol{T}$ terms have been often suppressed in the past together with their Galilean partners $\overset{\leftrightarrow}{J}{}^2$ (cf. e.g., Ref. [61]). However, the error associated to the suppression of the $\boldsymbol{S} \cdot \boldsymbol{T}$ terms in finite systems can be large. In Ref. [60] it was then shown that the lack of these time-odd terms can significantly alter the energy location of the GTR, which dominates the landscape in the (charge-exchange) 1^+ channel. It also turned out that the GTR collectivity, which, as known, experimentally absorbs the 60% of the Ikeda-Fuji-Fujita sum rule, can be badly affected by relatively strong (negative) values of the C_1^T coupling constant, a fact which explained the peculiar behavior of the SLy5 parametrization with respect to other Skyrme forces. Also, relatively too-weak C_T^T values (which depend on the t_1 and t_2 Skyrme parameters) would allow a too-strong mixing from the $\boldsymbol{S}^2$ terms (depending on t_0 and t_3, mainly fixed on bulk properties), unless the proper balance, or alternative formulations, are found. On such a basis, one conclusion of Ref. [60] was that the spin, velocity-dependent terms cannot simply be neglected as a rule and the parametrized EDFs rather need improved fitting procedures to model the dependence on the spin density, possibly including (further) constraints from collective properties.

Among the last developments in the central spin sector, extensions of the t_0-t_3 spin-dependent terms were proposed in Ref. [62], in connection to the spin phase transitions that are known to be predicted by effective approaches beyond the saturation density (cf. Ref. [63] and references therein).

The last remark of this section concerns superfluidity. An approximation still quite in use in order to include pairing correlations in TDHF consists in performing a BCS calculation at the mean-field level and evolving the dynamics on top of it. The sums in Eqs. (12) and (13) would, consequently, span the larger set of states that defines the pairing window, the expression of the ("normal") densities gain nontrivial occupation factors, and the energy functional is complemented by terms depending on the densities' "anomalous" counterparts [58].

A detailed description of the nuclear response would require a TDHFB approach. A full 3D-TDHFB is a demanding computational task. Some of the most advanced works of this type are represented by Refs. [64,65] and, for the Gogny case, by Ref. [66]. A full TDHFB implementation of the Skyrme functional, including also the tensor, is not yet available. The approximated and not fully self-consistent treatment

of superfluidity does not affect our conclusions on the p-h channel, although an extension which unifies the best efforts in both the p-h and p-p (particle-particle) channels is envisaged for the future.

1. Parameters, numerical tests and the center-of-mass correction

In this work we use the SLy5 force [67] with tensor parameters that were perturbatively defined in Ref. [55] and employed in subsequent applications starting with Ref. [68] (cf. also Ref. [69] and references therein). As known, the Lyon forces, which, in particular, received constraints also from microscopic calculations of the neutron matter equation of state, were tailored to improve the isovector channel of the effective interaction and, thus, the description of exotic systems. Like other works, we also employ the force T44 of Ref. [7], characterized by some different features. For example, the central + tensor isovector coupling constant $C_1^{J_1,c+t}$ of T44 vanishes and consequently, in the spherical limit, one is left with the isoscalar tensor contribution only. Moreover, for all the terms mentioned in the previous section (J_0^2, $\boldsymbol{J}^2$, $\underline{J}^2$, $\boldsymbol{S} \cdot \boldsymbol{T}$, $\boldsymbol{S} \cdot \boldsymbol{F}$, $\overleftrightarrow{J}^2$), the like ($C_0^T + C_1^T$) and unlike ($C_0^T - C_1^T$) particle tensor contributions to the mean-field operator have the same sign, at variance with the SLy5 case, where they are systematically opposite each other (see Table I).

The SLy5 and T44 forces have strictly negative central C_T^T coefficients, a quite common feature of the standard Skyrme sets (cf. Table II in Ref. [70]). They are relatively strong for both cases (with a different C_0^T/C_1^T ratio), so the effects from some of the newly implemented terms are expected to be emphasized with respect to other choices. With the inclusion of the tensor, the C_T^T coupling constants remain negative; the SLy5 ones receive a large reduction (90% and 84% for C_0^T and C_1^T, respectively), while the T44 $C_0^T + C_1^T$ and $C_0^T - C_1^T$ combinations are both strengthened in absolute value (see Table II of this work).

In the pairing sector, an (isovector) volume pairing force was implemented. For ^{120}Sn we set its (neutron-neutron) strength to the value $V_0(n) = 243$ MeV fm^3; in such a way,

TABLE I. Central and tensor coupling constant for the J_0^2, $\boldsymbol{J}^2$, $\underline{J}^2$, $\boldsymbol{S} \cdot \boldsymbol{T}$, $\boldsymbol{S} \cdot \boldsymbol{F}$ and $\overleftrightarrow{J}^2$ terms, according to the isospin formulation for the energy density functional. All the values are in MeV fm^5.

| | SLy5 | | T44 | |
	Central (c)	Tensor (t)	Central (c)	Tensor (t)
C_0^T	−15.67	14	−59.01	−24.40
C_1^T	−64.53	54	−52.03	20.81
$C_0^J = C_0^{J2}$	15.67	7	59.01	−12.20
$C_1^J = C_1^{J2}$	64.53	27	52.03	10.41
C_0^F	0	−42	0	73.19
C_1^F	0	−162	0	−62.43
C_0^{J0}	5.22	23.33	19.67	−40.66
C_1^{J0}	21.51	90.	17.34	34.69
C_0^{J1}	7.83	−17.50	29.50	30.50
C_1^{J1}	32.27	−67.50	26.01	−26.01

TABLE II. A_T (first line) and B_T (second line) coupling constants for the SLy5 force and, within parenthesis, T44 when the tensor is switched off ("central") or retained. All the values are in MeV fm^5.

	Central (c)	Tensor (t)	$c + t$
$C_0^T + C_1^T$	−80.20 (−111.03)	68.0 (−3.59)	−12.20 (−114.62)
$C_0^T - C_1^T$	48.87 (−6.98)	−40.0 (−45.21)	8.87(−52.19)

the SLy5 calculations including the $\overleftrightarrow{J}^2$ terms well reproduce (<1% of discrepancy) the experimental neutron pairing gap (1.32 MeV) obtained with the standard mass formula [71]. The associated energy cutoff is such that, as rule of thumb, only one extra major shell is included in the BCS space. In the following, we will refer to the choice $V_0(p) = V_0(n) = 243$ MeV fm^3 as "pairing set 1" in order to distinguish it from other sets discussed later in connection to heavier nuclei. In this work, we do not stick to the isospin invariance in the pairing channel adopted by some of us in the past [72] and we separately fix the proton and neutron pairing strengths.

The model space in the static calculations is a cubic box of 24^3 fm^3 with the commonly employed 1-fm grid step. A one-half reduction of the grid spacing would reproduce the HF single-particle spectrum with a better precision, causing variations from tens to 100–200 keV on single-particle energies in ^{16}O (which do not affect the features of the giant resonances we are interested in), but it would importantly enlarge the computational time of the dynamical simulation. We consider the standard choice of 1 fm to be a good trade-off for our purposes. In particular, the convergence in the static was checked, as usual, by looking at the stability of the single-particle energies.

The dynamic calculations were performed with reflecting boundaries over the same grid of the static case but extending the box side parallel to the boost direction to 64 fm for the lightest systems. In the other cases, a smaller squared box was used to save computational time which, together with the other model-space parameters, had been employed in previous calculations [73]. The box size, the simulation time length, and the boost strength, chosen small enough to stay in the linear regime, minimizing the particle emission but without being dominated by numerical noise, must be considered mutually dependent parameters, properly chosen to avoid unwanted effects from particle reflection. The choice for the input parameters can also be tested by checking the absence of unphysical fluctuations in the particle number or against the stability of the response computed in a reduced volume when rescaling the box size. The tests were successfully performed by looking at the heaviest nuclei.

The numerical accuracy was also checked by observing the free motion of a single ground-state nucleus on the grid, the typical test for the Galilean invariance. The nucleus in the starting rest condition is boosted by an external force and simply put into translation without, ideally, internal excitation. First, one notices that in the simple spin-saturated ^{16}O, the contribution to the total energy from the spin current $\overleftrightarrow{J}$ is expected to be zero, the same occurring for the energy contributions associated to the time-odd terms. Simulating the

translation, the former quantity turns out to be of the order of 10^{-4} MeV and it oscillates in time at the 10^{-5}-MeV level, while the HF single-particle energies change by a few tens of keV with respect to the "basic" calculation that neglects the $\overleftrightarrow{J}^2$ terms. The most important error source is due to the choice of the grid spacing size: the accuracy improves by one order of magnitude after a one-half reduction of this parameter. In order for the functional to be analytically Galilean invariant, the inclusion of the contributions associated to the pseudotensor $\overleftrightarrow{J}$ requires, as said, the $S \cdot T$ ones too, and, in the presence of the tensor, the $S \cdot F$ ($S \cdot G$) terms as well. In this system all the time-odd terms vanish with accuracy higher than the $\overleftrightarrow{J}^2$ terms, leaving no trace on the single-particle spectrum even at the eV level.

The last remark concerns the center-of-mass correction to the kinetic Hamiltonian term. In all our calculations, the total center of mass of the system at rest is located at zero—and it is expected to remain fixed if a purely internal excitation is produced. The simple one-body approximation was included when fitting the SLy5 force, so one should keep the correction active in the static HF. Concerning the dynamics, it is known [74,75] that conceptual problems about the definition of the mass of the system arise in TDHF, in relation to processes involving more than one fragment (fusion, fission, and collisions in general). When simulating giant resonances in TDHF, one needs to deal with the mass dispersion which accompanies the deexcitation process. Some other authors computing the GDR [20] choose to apply the center-of-mass correction to the mass distribution in the whole model space, considering the particle number as a constant in the time-space. Other practical recipes can be tried; we ran a few test cases in order to compare a calculation (YN) including the center-of-mass in the static, but not in the dynamic, thus some self-consistency breaking is introduced, a calculation (NN) that neglects it also in the static and the one (YY) accounting for the center of mass at both stages, with a constant mass number equal to the corrected static one. All these cases contain approximations, but we wanted to outline which is the least worst choice. The outcome from this comparison is represented in Fig. 1, where the isovector dipole response in ^{16}O is represented in the time (three horizontal plots) and energy domain (big plot), with arbitrary vertical scales. The total center-of-mass motion (obtained from the expectation value of the lowest-order isoscalar dipole operator $\hat{O}_{1-00}$, defined analogously to $\hat{O}_{1-01}$, but with τ_z replaced by I_τ, the identity operator in the isospin space) is plotted as well (dashed line). In the YN calculation the presence of a drift of the system is recorded and it is possible to notice the associated spurious concentration of strength at low energies. The difference between the NN and the YY calculations turns out to be small with the employed parameters in the linear regime.

III. RESULTS

As previously recalled, the isovector giant dipole resonance, which characterizes the experimental cross section more markedly than other vibrational states, is the first nuclear collective excitation which was discovered in photonuclear
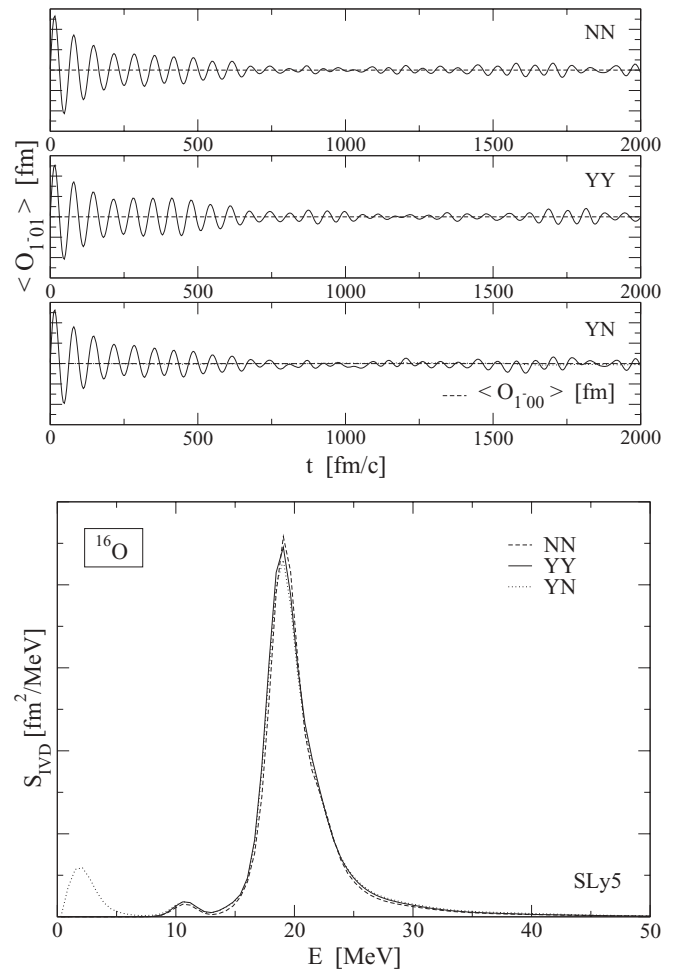

FIG. 1. Isovector dipole (IVD) response in ^{16}O in the time domain (NN, YY, and YN panels) and after the Fourier transform (big panel). The comparison among calculations including the center-of-mass correction everywhere (YY), nowhere (NN), and in the mean-field, but not in the dynamical evolution (YN), is shown. The vertical scale is arbitrary. For each calculation, the expectation value of the lowest-order isoscalar dipole operator is reported as well (dashed line).

reactions in the 1940s (cf. Ref. [76]) and imagined by A. Migdal in 1944 [77] in connection with the nuclear matter polarizability. The microscopic interpretation in terms of the (overall repulsive) residual effective interaction, able to explain the collective motion as superposition of nucleons undergoing particle-hole excitations, was achieved only 20 years later. Since that time, many experimental data have become available from a wide range of events, together with an extensive theoretical investigation. Forty years after the first observation, evidence of finite-temperature dipole modes taking place in a compound system from a heavy-ion collision were also found [78]. Some features of the GDR vary with temperature (like the size of the deformation and the width), while the centroid energies tend to remain stable.

The study of the zero temperature modes, the equivalent of the Landau zero sound, represents a useful way to explore the nuclear structure and also to identify features of the

intra-medium N-N interaction, testing how the current models perform. The main purpose of the current work is to analyze the effect of the Skyrme-tensor functional on (harmonic) dipole states set on top of the ground-state, although, in the absence of the study of the potential energy dependence on the deformation, the static mean-field is not guaranteed to correspond to the global minimum. In particular, in some cases, triaxiality is forced for explorative purposes. We leave for the future the investigation of finite-temperature events, which are important in connection to heavy-nuclei reactions [79] and in astrophysical environments.

In this section, the isovector dipole response from TDHF is presented for some benchmark nuclei with a mass number ranging from 16 to 238 having, or led to assume, different shapes. As is well known, the IVD response in axially deformed nuclei is characterized by a splitting related to the anisotropy of the single-particle motion: the experimental cross section

$$\langle \sigma_{1^-} \rangle(E) = \tfrac{1}{3}\sigma_{|1^-,0\rangle}(E) + \tfrac{2}{3}\sigma_{|1^-,1\rangle}(E) \qquad (32)$$

is a statistical average of the $|J^\pi, K\rangle = |1^-, 0\rangle, |1^-, 1\rangle$ modes, respectively associated to oscillations of protons against neutrons along ($K = 0$) and perpendicularly to ($K = 1$) the symmetry axis (see Fig. 2). Analogously, the cross section of giant resonances induced in triaxial nuclei is expected to break up into three contributions associated to the three characteristic lenghts of the system (k). Each distribution can be fitted with a Cauchy-Lorentz probability density function

$$\sigma(E) = \sigma_0 \frac{\tilde{\Gamma}^2}{(E - E_0)^2 + \tilde{\Gamma}^2}, \qquad (33)$$

where $\tilde{\Gamma} = E\Gamma$, with Γ being the scale parameter, E_0 the peak location, and σ_0 the corresponding height. From the
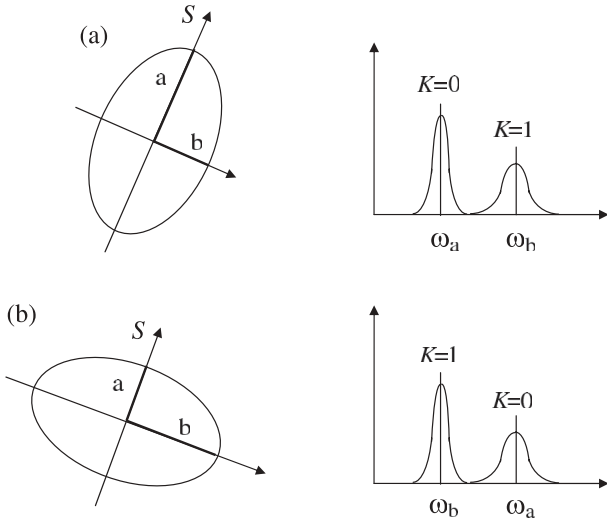

FIG. 2. Schematic representation of a prolate (a) and an oblate (b) nucleus and the relative position of the GDR $K = 0$ and $K = 1$ centroid energies, with a possible appearance due to the spreading (scales arbitrary; the height of the peak centered around ω_b needs to be doubled when comparing to the experiment). The half-axes are labeled consistently with Eq. (34). The symmetry axis (S) points toward the top.

TABLE III. Comparison between the empirical ratios (second column) of the dipole $K = 1$ and $K = 0$ energies, based on Eq. (34) and the nuclear size from the static Hartree-Fock approximation, and the corresponding TDHF predictions (third column) from the SLy5 force, with centroids evaluated in the whole energy range.

^{A}X	$(\overline{E}_1/\overline{E}_0)_{\text{emp}}$	$(\overline{E}_1/\overline{E}_0)_{\text{th}}$
^{24}Mg	1.385	1.332
^{28}Si	0.757	0.758
^{238}U	1.244	1.240

data, one can extract information regarding the type of deformation (triaxial or prolate, oblate shape) and its size, respectively represented by the so-called Hill-Wheeler parameters $\gamma = \arctan \sqrt{2}\beta_{22}/\beta_{20}$ and $\beta = \sqrt{\beta_{20}^2 + 2\beta_{22}^2}$, built up from the dimensionless quadrupole deformation coefficients $\beta_{2\mu} = \frac{4\pi}{5} \frac{\langle Q_{2\mu} \rangle}{A\langle r^2 \rangle}$. The splitting between the various k modes can be described by the shift between the centroid energies $\overline{E}_k = m1_k/m0_k$, computed as the ratio between the energy and non-energy-weighted sum rules (EWSR and NEWSR) for each k component (we will denote the centroid energy of the whole strength distribution by $\overline{E}$). The splitting is experimentally visible if the nucleus is far enough from the spherical shape ($\beta = 0$) and if it is not masked by other effects [80].

A macroscopic description of the deformation splitting is provided by the hydrodynamical model. Depicting the nucleus as a spheroid with eccentricity $a^2 - b^2$, where the semiaxis a is aligned with the symmetry axis, one has, in particular, the empirical relation for the quantity $\overline{E}_1/\overline{E}_0$ (see Ref. [76] and references therein)

$$\frac{\omega_b}{\omega_a} = 0.911 \frac{a}{b} + 0.089, \qquad (34)$$

where ω_b and ω_a are the oscillation frequencies of the liquid drop induced by an external perturbation along the given directions. Table III compares, for ^{24}Mg, ^{28}Si and ^{238}U, the (SLy5) TDHF centroid energy ratio with the right-hand side of Eq. (34) based on the HF geometry, with the result that the expectation from this empirical evidence is quite well fulfilled. Similarly, the centroid energies can be empirically described in presence of triaxiality [81].

Figure 3 shows the comparison between the theoretical centroids (for all the considered nuclei, despite the deformation) and the predictions from empirical fits. The behavior of the GDR energy when varying the mass number is parametrized like $\hbar\omega \sim 31.2A^{-1/3} + 20.6A^{-1/6}$ according to the Berman-Fultz (BF) model, which is expected to be more appropriate for spherical light-medium nuclei (typically $A < 100$), where the correction for the surface ($\propto A^{-1/6}$) is more important, or by $\hbar\omega \sim 79A^{-1/3}$ MeV from the Steinwedel-Jensen (SJ) formula (see references in Refs. [82,83]). In particular, for each value of the mass number the main plot displays the empirical prediction which is closest to the performance of the SLy5 force (the full trend from both models is reported in the inset). The BF formula turns out to be reproduced better than SJ up to ^{120}Sn. In any case, it is clear that the discrepancy with the result from Skyrme is quite high in the light nuclei; although
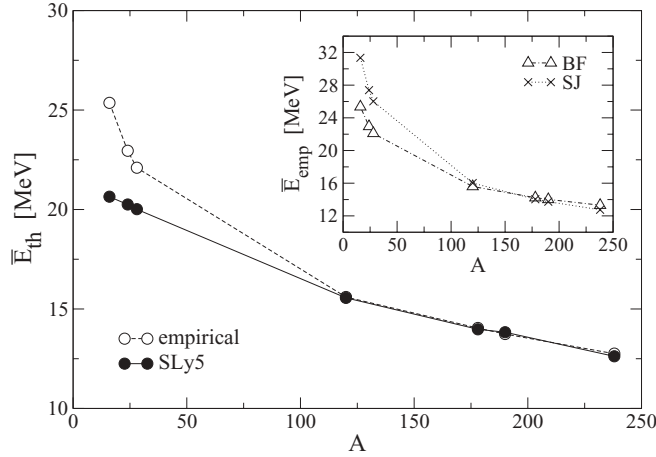
FIG. 3. Comparison between predicted (solid circles) and empirical (open circles) GDR energies through different regions of mass. The theoretical numbers correspond to the total centroids $\overline{E}$, while the empirical points are from the BF or SJ model, as indicated in the main text (the complete empirical trends are shown in the inset).

FIG. 4. Isovector dipole (IVD) strength distribution in ^{16}O obtained for different truncations of the SLy5 functional. The legends indicate the terms made active in the corresponding calculation, in addition to the "basic" version. Details in the main text.

other sets can better perform in such cases, the simultaneous reproduction of the GDR across different mass regions of the periodic table is a long-standing problem [84] (see also Ref. [75] and references therein).

As previously anticipated, in this paper various truncations of the SLy5 and T44 Skyrme functional are considered, with the purpose of studying how the central spin-dependent and tensor terms manifest themselves on the nuclear response. Relative effects from the p-h channel are, therefore, discussed. In any case, particular attention is reserved to the definition of the pairing force. It should be mentioned that the predictions for the percentage of total EWSR exhausted in the finite energy intervals of interest are quite sensitive to the model parameters. Higher-precision calculations are possible in order to provide more robust estimates where needed.

Particular attention is payed to the central $\overleftrightarrow{J}^{\,2}$ terms (cf. Sec. II B), which had not yet been included in our model. In this work we will label the calculations obtained without the spin-current tensor and with none of the time-odd (with the exception of the time-odd spin-orbit) nor tensor terms "basic." In all the plots displaying the calculated IVD transition strength distribution, which is measured in fm^2 unless an artificial smoothing is introduced, the scale on the vertical axis has been normalized to the highest peak produced, for the considered nucleus, in the SLy5 calculation including the central $\overleftrightarrow{J}^{\,2}$ terms (labelled by J_c^2 or simply J^2. In the plots where the $K = 0$ and $K = 1$ components are separately plotted, no relative factor 2 is included).

The results have been extensively verified. Comparisons to other theoretical works or experimental data are provided where available.

A. ^{16}O

The first case considered is ^{16}O, a historically widely used benchmark for TDHF calculations due to the low demand of computational complexity. Desp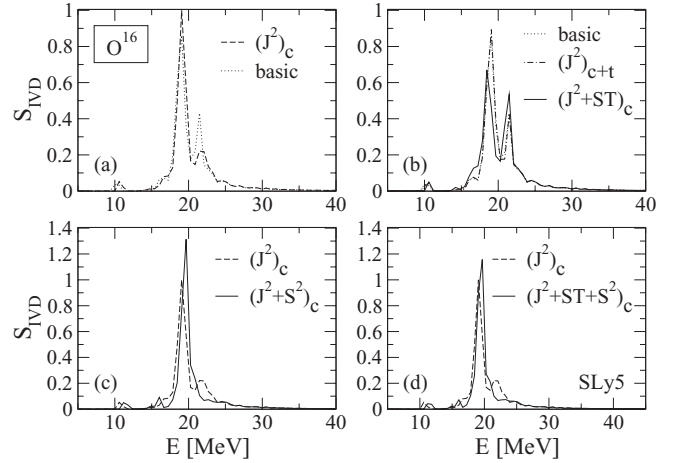ite the limitations of the mean-field approach and the known problems with reproducing the location of the GDR in light systems, it still is a good candidate to highlight some features of the Skyrme functional. In fact, the residual interaction is expected to affect how the strength is distributed in light nuclei more markedly than in heavier systems, where, by a microscopic point of view, more single-particle levels are involved in the process and shell-dependent effects tend to average out.

The calculated isovector dipole in ^{16}O mainly lies between 15 and 25 MeV. Figure 4(a) shows the response from the SLy5 functional including the central $\overleftrightarrow{J}^{\,2}$ terms (dashed line), in comparison to the "basic" calculation previously defined (dotted line). They produce a shift to higher energy of both of the two main bumps which characterize the response, which are peaked at 19.1 and 22.1 MeV. The most prominent effect is obtained for the smaller peak at higher energy, the strength of which is reduced by a factor 2 in the more complete calculation.

An evident change on the strength function appears when including the $\overleftrightarrow{J}^{\,2}$ Galilean invariant partner in the functional, that is the $S \cdot T$ contribution, which increases the response fragmentation for both the Skyrme forces [Fig. 4(b)]. For the SLy5 case, such calculation produces two new bumps of almost equal size, which are peaked at 18.5 and 21.5 MeV. This is the case which qualitatively looks more similar to the experimental cross section, which, in low-resolution experiments, displays two main structures around 22 and 25 MeV [83]. However, analyses of the microscopic structure in such 1p-1h limit are required to add more information. Figure 4(d) shows the calculation obtained when including also the S^2 terms and confirm their capability to increase the strength of the dipole response, overcoming the effect of the $S \cdot T$ terms. As a matter of fact, as a consequence of the action of the spin-squared terms, there is basically one single centroid with the highest peak at 19.7 MeV, showing an enhanced transition probability and raised in energy with respect to the J_c^2 calculation. The outcomes described above are similarly obtained with the T44 force (Fig. 5). The "aggregating" behavior of the S^2
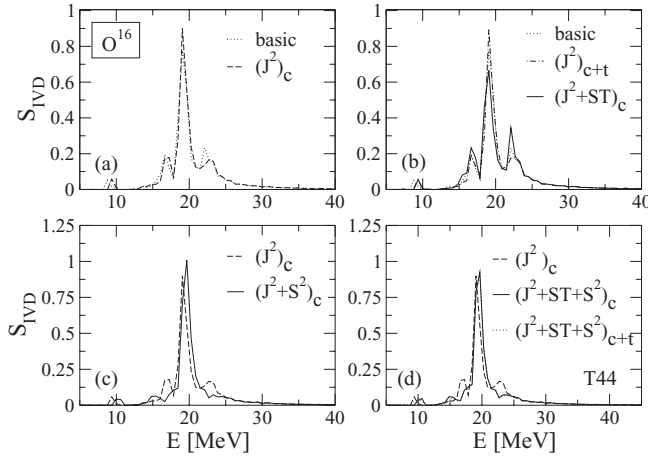
FIG. 5. Same as described in the caption to Fig. 4 for the T44 force.

ingredient was already observed, without the $S \cdot T$ terms (c), in Ref. [20], where the TDHF dipole response in ^{16}O and Be isotopes was analyzed with the SIII force, but no systematic calculations were carried on. In general, in a p-h view, the spin-squared terms, including the rearrangement due to the density dependence, are able to couple spin-flip ($\uparrow\downarrow$, $\downarrow\uparrow$), which do not directly contribute to the IVD transition amplitudes, and non-spin-flip ($\uparrow\uparrow$, $\downarrow\downarrow$) particle-hole pairs with configurations of the same family, and, to some extent, to also mix them up. By suppressing the C_T^S one-body contribution that depends on the spin ladder operators, the effect from the spin-squared terms on the whole distribution is lost in our TDHF calculations and one recovers the two-peaked structure of the J_c^2 run (the rearrangement has no effect). This finding is possibly related to the specific shell structure of ^{16}O. Further analyses will be discussed in the future.

The results obtained by adding the tensor terms associated to the spin current $\overleftrightarrow{J}$ to the central ones [hereafter labeled by J_{c+t}^2 like in Fig. 5(b)] turn out to be identical, or displaying a negligible difference, to the "basic" version which does not include any of the new terms. The inclusion of the tensor to the $S \cdot T$ contribution does not produce an appreciable effect either.

The information about the SLy5 centroid energies for the different types of calculations are summarized in Table IV, together with the percentage of total EWSR correspondingly exhausted. They are evaluated in the intervals 17–20 MeV (18–21 MeV for the T44 force), labeled by (I), where the main peak from the J_c^2 calculation is located. The information about the transition strength that is left between 20 and 24 MeV (II) is given as well. For the calculations including the S^2 terms (last two lines), the considered interval is 17–22 (17–23) MeV: the strength is collected in a single bump absorbing more than the 74% of the total EWSR. In all the calculations, a small fraction of strength is concentrated around 10 MeV. The total centroid energy amounts to 20.6 MeV (20.8 MeV) for the SLy5 (T44) force.

Studying the spin response is not the aim of this paper; nevertheless, we tracked in time the expectation value of the operator $O_{1-11}^K = \sum_i Dg_{1K}(\boldsymbol{x}_i, \omega_i)\tau_z(i)$, where $g_{1K}(\boldsymbol{x}, \omega) =$

TABLE IV. Isovector dipole centroid energies in ^{16}O for various types of calculations not including the tensor. "Basic" means that none of the terms specified in the subsequent lines have been included. The considered intervals are [17,20] MeV (I) and (20,24) MeV (II) for SLy5 ([17,22] MeV and (22,24) MeV for the last two rows), [18,21] MeV for T44 ([17,23] MeV). The percentage of total EWSR exhausted in each energy range is reported within parenthesis.

	SLy5 (I)	SLy5 (II)	T44
Basic	18.94(52.3%)	21.86 (28.2%)	19.40 (52.1%)
J^2	19.05(57.0%)	22.08 (23.7%)	19.45 (54.4%)
$J^2 + ST$	18.71(43.6%)	21.73 (34.8%)	19.34 (45.6%)
$J^2 + S^2$	19.66(75.2%)	23.23 (5.20%)	19.72 (72.3%)
$J^2 + ST + S^2$	19.56(74.1%)	23.28 (5.90%)	19.62 (71.6%)

$\mathcal{Y}_{1K}(\boldsymbol{x})|\boldsymbol{x}|\sigma_z(\omega)$. This corresponds to

$$\langle \hat{O}_{1-11}^K \rangle(t) = \frac{\tilde{D}}{2} \int \lambda \big[S_z^{(n)}(\boldsymbol{x}, t) - S_z^{(p)}(\boldsymbol{x}, t) \big] d\boldsymbol{x}, \quad (35)$$

where $S_z^{(n)}(\boldsymbol{x}, t) - S_z^{(p)}(\boldsymbol{x}, t)$ is the time-dependent spin-isovector density $\rho_{11} = (\rho_{n\uparrow} - \rho_{n\downarrow}) - (\rho_{p\uparrow} - \rho_{p\downarrow})$. The signal takes place at a scale which is several orders of magnitude smaller than the dipole response. For some truncations of the Skyrme EDF, regular oscillations occur from an early stage [solid line in Fig. 6(b)] and appear to grow up in time. The plot is for SLy5 and the same has been found for other cases. We verified that within the time length considered, and well beyond, such behavior, which is not enhanced when reducing the box size, is small enough to not influence the observed dipole strength. In particular, the oscillations are not larger than the spurious total center-of-mass motion, represented, for the same calculation, by a dotted line in all the three panels. This, in turn, is two orders of magnitude smaller than the worst case (YN) that was shown in Fig. 1 (dashed line in the bottom
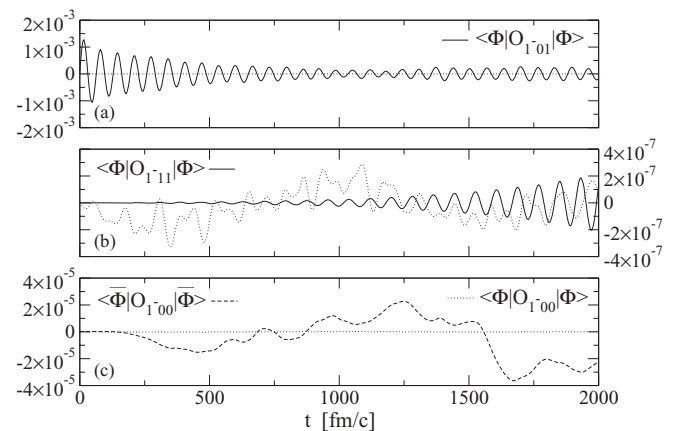

FIG. 6. Time dependence of the dipole response [solid line in (a)] and of the spin-dipole component [solid line in (b)] described in the main text, for SLy5 in ^{16}O. The total center-of-mass displacement (lowest-order isoscalar dipole operator) is plotted as a dotted line in all the three panels. In panel (c), the same quantity corresponding to the worst (YN) case of Fig. 1 is reported (dashed line). All the quantities are directly comparable and measured in fm.

panel) and comparable to the NN and YY cases. Further studies are underway.

B. ^{24}Mg

The lightest axially deformed system we present is ^{24}Mg. The pairing correlations are negligible and the nucleus has a prolate shape; hence, one main splitting of the response arising from the deformation is expected, with the $K = 0$ mode, associated to oscillations along the symmetry (major) axis, being less energetic than the $K = 1$ one.

The dipole calculations performed with the new terms present some important pathologies when using the T44 parametrization and especially when the boost is applied along the major axis: with the new terms, the system displays spurious excitations, enters the nonlinear regime, and is led to fission or explosion. This is the case when adding the tensor from the $\overleftrightarrow{J}$ spin current: the dipole oscillations are dramatically enhanced and the system splits up as a result of an inelastic collision. Rotational effects can arise as well, as in the $J^2 + S^2$ model with no tensor, where the dynamic is similar to a fusion state after a noncentral collision. With the $J^2 + \mathrm{ST} + S^2$ model, octupole deformations appear on top of the dipole oscillations. When the boost is applied along the perpendicular direction, the pathologies due to the inclusion of the S^2 terms are largely reduced when the $S \cdot T$ terms are added as well.

When using the SLy5 force, it is necessary to run the simulation longer (at least for a time doubled with respect to the T44 $J^2 + S^2$ case) to face the same kind of instabilities, which manifest far outside the time window considered in this work, without affecting the results. These are shown in Fig. 7. Nonzero signal is mainly visible between 13 and 30 MeV, with a narrow peak associated to the $K = 0$ mode located at 15.8 MeV (practically unchanged when switching on/off the tensor and time-odd terms of the functional), and a broader bump associated to the second characteristic length of the system ($K = 1$), with a narrower structure in the 18–23 interval (II). The central J^2 model performs similarly to the "basic" one. For the runs without tensor, the plot presents a pattern similar
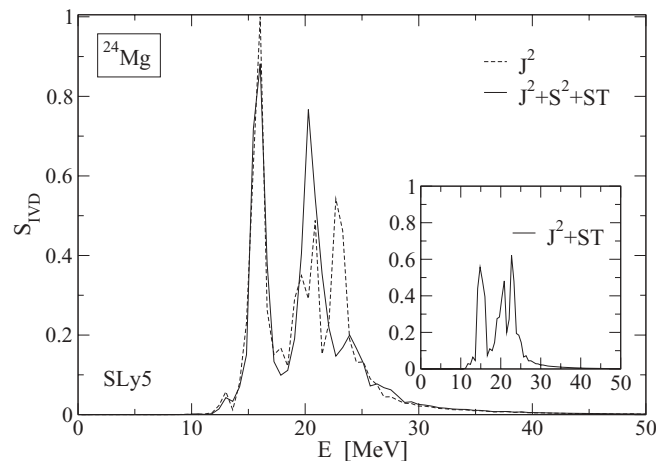
TABLE V. Isovector dipole centroid energies in ^{24}Mg for various types of SLy5 calculations not including the tensor, evaluated in the intervals [0,18) MeV (I) and [18,23) MeV (II) and in the larger [18,26] MeV window (III). The exhausted percentage of the total EWSR is listed within parentheses.

SLy5	I	II	III
J^2	15.81 (30.0%)	20.14 (31.5%)	21.78 (56.5%)
$J^2 + S^2$	15.85 (29.9%)	20.74 (44.2%)	21.42 (56.8%)
$J^2 + \mathrm{ST} + S^2$	15.79 (30.1%)	20.58 (42.0%)	21.37 (55.5%)

to that of Oxygen: the S^2 terms are able to reduce the spreading of the dipole response with respect to the central J^2 calculation (dashed line), while the $S \cdot T$ terms work in the opposite direction (full central calculation $J^2 + \mathrm{ST} + S^2$ represented by a solid line). In the inset, the $J^2 + \mathrm{ST}$ calculation is separately drawn.

All the information about the centroid energies computed in the intervals of interest are listed in Table V, together with the corresponding fraction of exhausted EWSR (see the caption for details). The calculation obtained by adding only the $\overleftrightarrow{J}^2$ terms to the "basic" one places in interval II about 10% less than the energy-weighted strength of the other cases, because the $K = 1$ mode is fragmented at higher energies (still within interval III). The total centroid amounts to 20.2 MeV for all the considered truncations of the SLy5 functional. The inclusion of the time-odd terms reduces the overall deformation splitting by 300–400 keV, which globally amounts to about one-half of what is predicted by the Gogny-based QRPA of Péru and Goutte [85]. This change is only due to the residual effects in the p-h channel, since the time-odd terms vanish in the ground-state and do not alter the single-particle spectrum. Our outcome is similar to the SkM* [86] (Q)RPA result with no tensor presented by Ref. [87] (same deformation parameters and rms are obtained in the ground-state).

C. ^{28}Si

^{28}Si is a system comparable to ^{24}Mg in mass but with different deformation properties. Both the SLy5 and T44 forces predict an oblate shape ($\gamma = 60°$), with a β parameter that, with the second force, is about 30% weaker when the central $\overleftrightarrow{J}^2$ contribution is not included ($\beta = 0.19$ in the "basic" versus $\beta = 0.26$ of the J_c^2 case); it increases by a further $\sim$10% when the tensor is switched on. The variations are smaller in the SLy5 case ($\beta = 0.28 \pm 0.01$ for the three calculations), with the $\overleftrightarrow{J}^2$ terms still enhancing the deformation.

Figure 8 shows how the linear response changes between the J^2 run, where, we recall, the (central) $\overleftrightarrow{J}^2$ terms are self-consistently included in both the static and the dynamic, and the "basic" version where they are neglected at both levels. The upper (bottom) panels are for the SLy5 (T44) force and the $K = 1$ and $K = 0$ modes are separately computed at the left- and right-hand sides, respectively. It is possible to notice that the response around 22 MeV receives contribution from both the $K = 0$ mode and the Landau spreading of the $K = 1$ component. For the T44 case, the spin-current terms enlarge
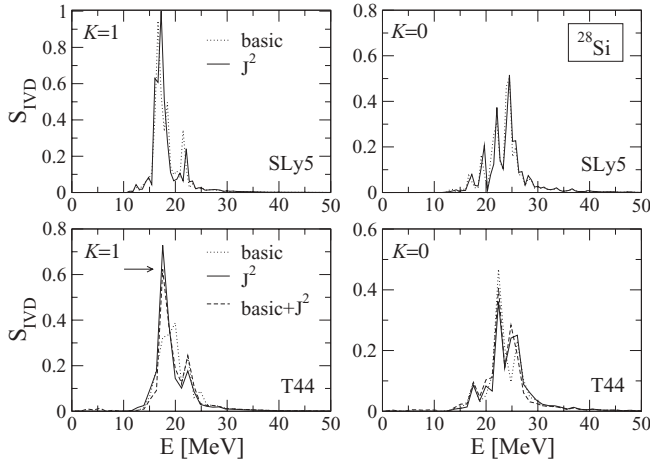

FIG. 7. IVD response from the SLy5 force in ^{24}Mg for the calculations specified by the labels. Only central terms are included.

FIG. 8. $K = 1$ (left panels) and $K = 0$ (right panels) components of the IVD strength distribution in ^{28}Si from the SLy5 (top) and T44 (bottom) force. The comparison between the "basic" and the (central) J^2 calculation is shown. The basic $+ J^2$ run has been obtained by suppressing the $\overleftrightarrow{J}^2$ terms in the ground-state only. The arrow indicates the height of the main peak in the latter case.
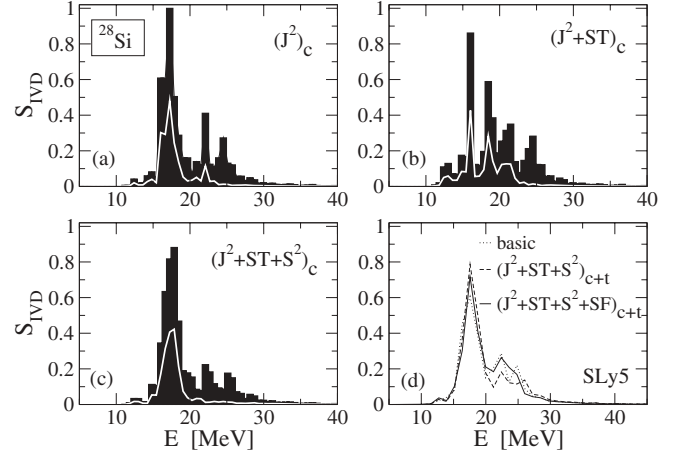

FIG. 9. IVD response in ^{28}Si for various types of SLy5 calculations. The white profiles show the (rescaled) profile of the response perpendicularly to the symmetry axis ($K = 1$).

the splitting by 1.4 MeV, since the $K = 1$ centroid lowers from 20.5 to 19.5 MeV, while the $K = 0$ one increases by 400 keV, as reported in Table VI; as a consequence, the ratio between the centroid energies decreases by 6% (third column). The empirical estimates of Eq. (34) are listed in the last column for comparison. The effect from the SLy5 force is less pronounced, but similar.

As said, a useful tool to investigate how the energy functional reproduces the nuclear response consists in performing not-self-consistent calculations where the underlying mean-field is obtained from a functional simpler than that used in the dynamic evolution. In such a way, one can disentangle effects arising from the static mean-field, including the change produced on the intrinsic deformation. By doing this in the T44 case, it is possible to see that the 1.4-MeV variation of the shift between the $K = 0$ and $K = 1$ modes can be explained in terms of the change produced on the ground-state, which, as said, is made more oblated by the $\overleftrightarrow{J}^2$. In fact, when turning the spin current on in a dynamical calculation performed on top of the "basic" mean-field (basic $+ J^2$), one obtains a profile similar to the fully self-consistent J^2 run (see the dashed lines in Fig. 8 for T44), but the gain in the energy splitting is practically lost and one recovers exactly the same energy

ratio of the pure "basic" case (a small fraction of strength can be noticed at low energies, below 10 MeV, due to the self-consistency breaking).

From Fig. 9, showing the total IVD strength from the SLy5 force, one can identify, once again, the opposite behavior of the central $S \cdot T$ (upper-right panel) and S^2 terms (lower-left panel) in redistributing the transition strength. Table VII displays the centroid energies computed below (interval I) and above (II) 20 MeV. With the S^2 ones, strength is pushed at higher energies. The $S \cdot T$ terms fragment the response, with the result that the main peak is lowered by 100 keV and some transition probability is now visible between 18.0 and 21.5 MeV.

Concerning the tensor, instabilities arise when including the $S \cdot F$ terms. In the case of the SLy5 force, these appear at the middle of the time length we have typically assumed. We still attempted to compare with runs where the C_T^F coupling constants are zero by halving the simulation time. This operation might lead to loose relevant information, although it turns out that, when repeating the same operation with the cases listed in Table VII, the relative differences between the calculations still hold. From Fig. 9(d), it seems the $S \cdot F$ terms produce an overall attractive effect. The same comparison between T44 calculations including the tensor is shown in Fig. 10. The $S \cdot F$ terms shift down the highest peak by a further ∼300 keV and also move strength ($K = 0$ mode) to

TABLE VI. $K = 1$ and $K = 0$ centroid energies from T44 in ^{28}Si, evaluated in the whole energy range, from the three types of T44 calculations of Fig. 8. The comparison with the empirical ratio of Eq. (34) is given as well.

T44	$\overline{E}_1$ (MeV)	$\overline{E}_0$ (MeV)	$(\overline{E}_1/\overline{E}_0)_{\text{th}}$	$(\overline{E}_1/\overline{E}_0)_{\text{emp}}$
Basic	20.45	24.38	0.839	0.837
J^2	19.45	24.79	0.785	0.780
Basic $+ J^2$	19.99	23.82	0.839	0.837

TABLE VII. Isovector dipole centroid energies in ^{28}Si for the SLy5 force evaluated below (I) and above (II) 20 MeV for the calculations listed in the first column (no tensor).

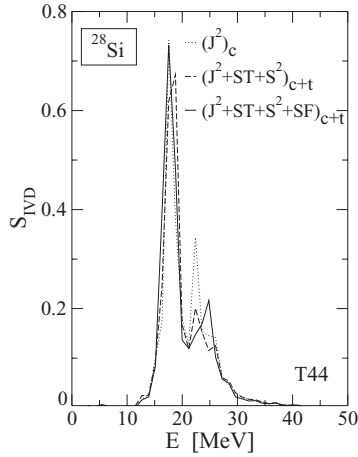| SLy5	I	II
J^2	17.13	25.16
$J^2 + \text{ST}$	17.02	24.85
$J^2 + S^2$	17.38	25.25
$J^2 + \text{ST} + S^2$	17.40	26.02

FIG. 10. IVD response in ^{28}Si for the T44 calculation listed in the legend.

higher energies. In any case, the role of these tensor terms should be further investigated.

D. ^{120}Sn

The next case under study is the spherical ^{120}Sn, where, at variance with the previous cases, pairing correlations are important and are modelled with the pairing parameters (set 1) introduced before. Superfluidity opens the channel to the $\overleftrightarrow{J}^2$ tensor terms also in the ground-state, preventing the $N = 70$, $Z = 50$ core from being spin saturated, although the system remains time-reversal invariant. Consequently, there is no contribution from the time-odd terms in the mean-field. While checking this, we noticed that the inclusion of the $\boldsymbol{S} \cdot \boldsymbol{T}$ terms may help the convergence in the static calculation when the squared spin density is turned on. When the $\overleftrightarrow{J}^2$ terms are switched on, the pairing gap changes by 1–2%, which is far from producing a relevant change on the main properties of giant resonances. When using the optimum SLy5 pairing set in connection to the T44 force, a pairing gap of 1.84 MeV is obtained. However, even a change of around +20% of the pairing strength ("pairing set 2"), which significantly alters the pairing gaps, would produce small variations on the response (cf. Fig. 11, left panel). There is, consequently, no need to further tune the pairing either when modifying the functional for a given force or when changing from SLy5 to T44.

The SLy5 strength distribution is characterized by two main peaks (cf. Fig. 12). The predictions for the centroid energy ($\sim$15.4 MeV, calculated in the 13.0–18.5 MeV interval) match the experimental value reported in Ref. [83] (cross-section data fitted in the 13- to 18-MeV range). The change produced by the new terms in this superfluid $A = 120$ nucleus is less evident than in the lighter systems. However, one can still notice [Fig. 12(b)] that the $\boldsymbol{S} \cdot \boldsymbol{T}$ terms (slightly) reduce the peaks' height ratio and produce an attractive effect on the centroids, at variance with that obtained when adding the $\boldsymbol{S}^2$ terms [Fig. 12(c)]. All the calculations modify the low-energy tail of the strength function (below 13 MeV), although these outcomes must be considered carefully, since the low-lying states, besides being sensitive to higher-order p-h correlations
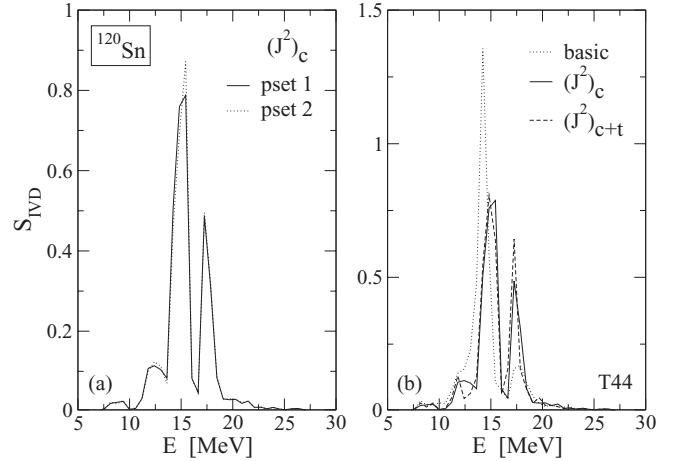

FIG. 11. Panel (a) shows the dependence of the IVD response in ^{120}Sn on the pairing sets "1" and "2" defined in the main text when using the T44 force. Panel (b) shows the effect of the inclusion of the tensor $\overleftrightarrow{J}^2$ terms (dashed line) in comparison to a calculation including only the central counterpart (solid line) and when none of them is taken into account (dotted line).

and pairing, can be particularly affected by numerical artifacts from the Fourier transform and spuriousities in the wave functions.

When the tensor $\overleftrightarrow{J}^2$ and $\boldsymbol{S} \cdot \boldsymbol{T}$ terms are made active, no noticable change on the strength function is introduced when SLy5 is used. This is not the case with the T44 force, where the J^2_{c+t} calculation differs somewhat (cf. Fig. 11, right panel). We finally notice that the two-peak structure always visible with the SLy5 force is lost when using the T44 set in the simplest "basic" calculation, where the distribution is shifted to lower energies, but it appears as soon as the $\overleftrightarrow{J}^2$ contribution is added.

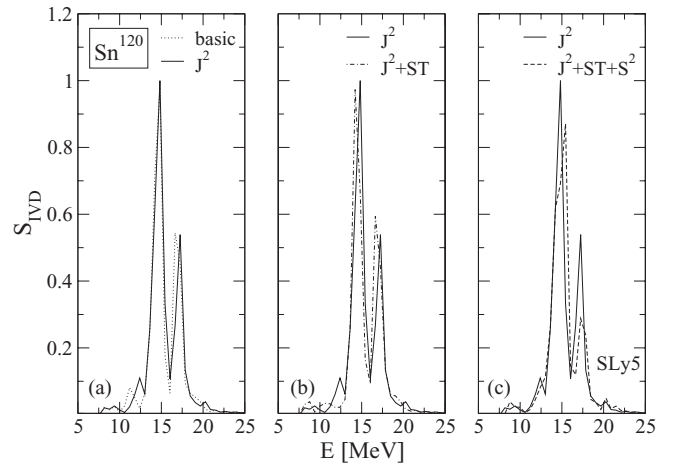FIG. 12. IVD response in ^{120}Sn from the SLy5 force (no tensor); the three panels show the change produced when including the $\overleftrightarrow{J}^2$ terms [panel (a), solid line], when also adding the Galileain invariant partners $\boldsymbol{S} \cdot \boldsymbol{T}$ [panel (b), dashed-dotted line] and when switching on the $\boldsymbol{S}^2$ ones as well [panel (c), dashed line].
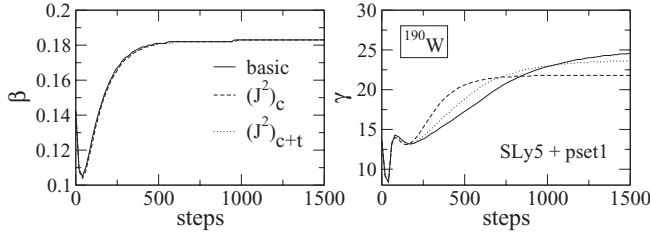
FIG. 13. Evolution of the deformation parameters β and γ in ^{190}W during the first stage of the iteration process in Hartree-Fock for SLy5. Different lines correspond to different runs complemented by the pairing force 1, as explained in the legend. β is adimensional; γ is measured in degrees.

E. ^{190}W

In triaxial nuclei the deformation leads to a more complex nuclear response when the system is excited. The intrinsic nuclear shape, which affects the dynamical response, results from the balance of different features of the intra-medium N-N force: on the one hand, various truncations of the Skyrme functional in the p-h channel can affect the deformation properties in the ground-state; on the other hand, (monopole) pairing correlations tend to drive the nuclear system towards a spherical shape and alter the deformation parameters as well, so the proper focus on the pairing force must be posed when studying intrinsically deformed systems where superfluidity plays a role.

The measurement of the E_{4^+}/E_{2^+} energy ratio, which is a good signature of shape transition, suggests that ^{190}W behaves like a triaxial rotor [88]. When using the optimum ^{120}Sn pairing force (set 1) in connection to the SLy5 functional, a triaxial shape is obtained from our calculations. The two panels in Fig. 13 show (an extract of) the evolution of the β and γ parameters in ^{190}W with the number of iterations with the SLy5 functional, for a "basic" calculation and when the spin-current pseudotensor is included (with and without tensor). This is an example where the inclusion of the $\overleftrightarrow{J}^2$ terms quicken the convergence. In particular, a 14% decrease of the γ value (21.8°) with respect to the "basic" calculation (25.3°) is produced. A SLy4 calculation obtained with no $\overleftrightarrow{J}^2$, with the same starting conditions, shows a γ parameter ($\gamma = 23.2°$) close to the J^2_{c+t} SLy5 one ($\gamma = 23.7°$). The β parameter does not change.

The type of truncation of the energy density functional can not only induce a variation of the deformation parameters for a given (local or global) minimum but also reverse the relative location in energy of different minima. For example, when the $\overleftrightarrow{J}^2$ terms are neglected in the functional based on the T44 + pairing 1 parameters, it is possible to identify one axially deformed and one triaxial solution, with an energy difference of 0.91 MeV, where the prolate configuration is the most bounded. By switching those (central) terms on, the situation is reversed, with the triaxial configuration becoming deeper than the prolate shape (with small variations of the β and γ parameters, respectively, amounting to $\sim$1% and $\sim$3%) by 1.42 MeV. This extra binding is mainly due to the fact that the (positive) energy contribution from the central $\overleftrightarrow{J}^2$ terms in the triaxial case (9.78 MeV) is 2.3 MeV weaker than in

TABLE VIII. Isoscalar + isovector Hartree-Fock energies (in MeV) from the central J_0^2, $\boldsymbol{J}^2$, and $\underline{J}^2$ terms of the T44 functional in the prolate ($\gamma = 0°$) and triaxial ($\gamma = 39.3°$) minima found in ^{190}W.

T44	ΔE_{J_0}	ΔE_{J_1}	ΔE_{J_2}
$\gamma = 0°$	$\asymp 10^{-7}$	11.951	0.157
$\gamma = 39.3°$	$\asymp 10^{-5}$	9.671	0.105

the axial state (cf. Table VIII where the three J_0^2, $\boldsymbol{J}^2$, and $\underline{J}^2$ components are separately shown).

Turning on the time-odd terms, Kramer's degeneracy is expected to be preserved. Their inclusion tends to make the convergence more difficult and the time-reversal invariance is easily broken; in particular, use of the T44 force requires effort to find suitable initial conditions. In some cases the problems are emphasized when the $\boldsymbol{S} \cdot \boldsymbol{T}$ terms and the $\boldsymbol{S}^2$ ones are included separately. We encountered a similar situation when changing the pairing parameters, including the values of 288.5 and 298.8 MeV fm^3 for the neutron and proton pairing strengths, respectively ("pairing set 2"). These are optimal parameters in connection to the SLy5 force, as they provide pairing gaps $\Delta_{n,p} \in 0.7$–0.8 MeV, which are much closer to the empirical estimates (0.859 and 0.740 MeV) than the quite small pairing gaps obtained with pairing set 1 ($\Delta_q \in 0.2$–0.4 MeV, $q = n, p$).

We noticed interesting variations on the deformation properties when changing the pairing force, with the same initial conditions (the same providing the triaxial solution when using pairing set 1). Figure 14 shows the outcome from "basic" T44 calculations based on the pairing sets considered in this work. If the choice of pairing set 2 leads, in this case, to a prolate axially deformed shape, by reinforcing the proton pairing strength by $\sim$15%, that is, up to 344.00 MeV fm^3 ("pairing set 3"), one triaxial minimum with $\gamma = 42°$ is constructed. Reversing such proton and neutron pairing strengths ("pairing set 3a") would force the system to converge to an oblate shape (dotted line; notice the spike around the 100th step).
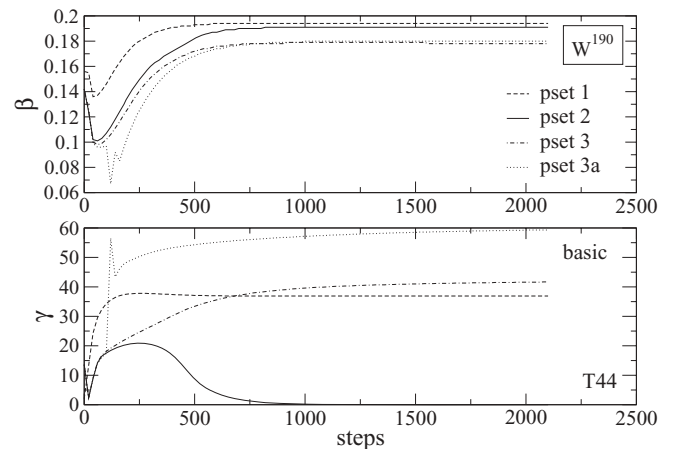

FIG. 14. Dependence of the deformation parameters of ^{190}W on the pairing force for the T44 Skyrme set with the iteration step number. The pairing sets used in this work are considered.
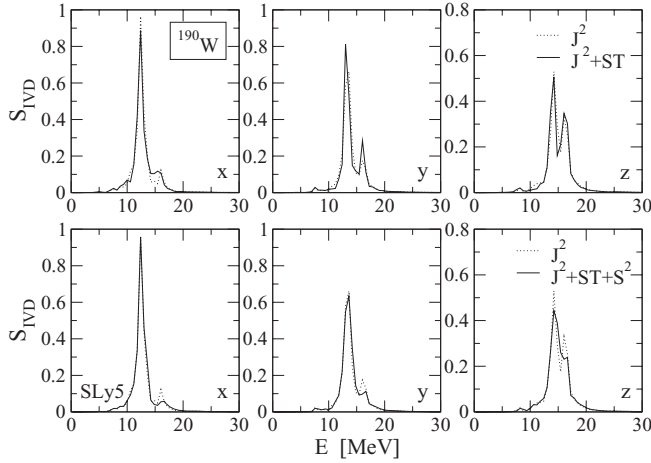
FIG. 15. IVD transition strength distribution in ^{190}W on top of a triaxial ground-state. The x (main axis), y, and z components are separately plotted for some truncations of the SLy5 Skyrme functional as described in the main text.

Concerning the projection of the linear response in the IVD channel, in a triaxial case we expect a three-modal response associated to the characteristic lengths of the nucleus. Figure 15 shows the transition strength distribution in ^{190}W from the SLy5 force along the x, y, and z Cartesian axis and for some truncations of the Skyrme functional. Each mode appears as a bimodal function, where the highest peak is respectively located at $\sim$12, 13, and 14 MeV and a weaker structure is around 16 MeV in all the panels. The latter bump becomes increasingly more important from x to z while the main peak reduces in height by $\sim$40%. Concerning the various functional terms, the $S \cdot T$ ones (three upper panels) produce an overall (small) attraction on the y and z components. The inclusion of the S^2 terms (three bottom panels) tends, instead, to remove the bimodal structure in all the components and the extra mixing places the (new) centroids at higher energy.

The comparison of the total strength distribution among three types of calculations including the tensor with the T44
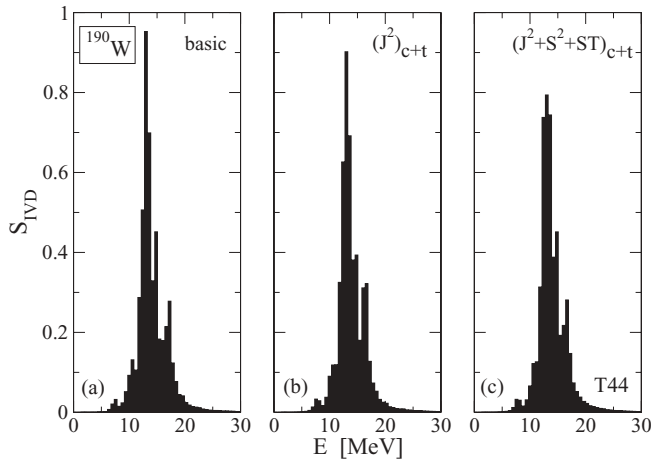

FIG. 16. IVD strength distribution in ^{190}W from the T44 force, in a "basic" calculation and when including the tensor at the J^2 and $J^2 + S^2 + ST$ level, as denoted by the legends.
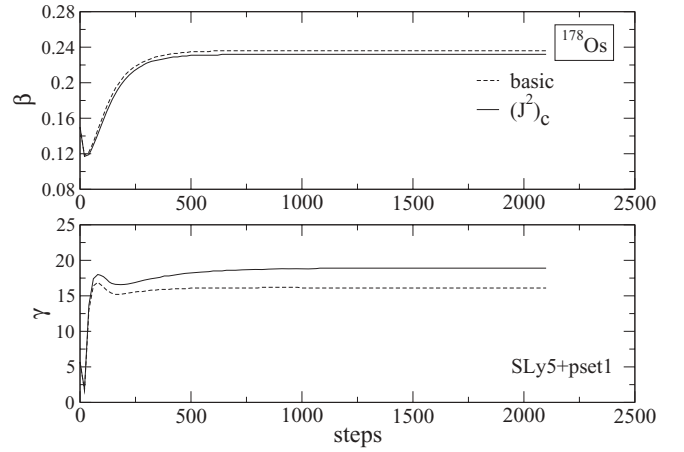

FIG. 17. Same as Fig. 13 for ^{178}Os.

force is shown in Fig. 16. The effect of the central + tensor contributions associated to the pseudotensor $\overleftrightarrow{J}$ [Fig. 16(b)], that is, from the central + tensor J_0^2, $\boldsymbol{J}^2$, and $\underline{J}^2$ terms of the functional, and to $S \cdot T$ (c) consists in a broadening of the response with respect to the "basic" [Fig. 16(a)] case. Although the inclusion of the tensor can help the numerics in some cases, no stable calculation including the tensor $S \cdot F$ terms is currently available in this nucleus.

F. ^{178}Os

Another system under study is ^{178}Os, which has been considered a good candidate for shape cohexistance (see Ref. [89] and references therein). As for ^{190}W, we exploit the γ-softness property to perform theoretical investigations by forcing triaxiality in some cases. In this system, both the empirical proton and neutron pairing gaps belong to the interval 0.91–0.93 MeV. Among the various pairing sets considered, force 2 still appears the most suitable, although the convergence is not trivially ensured, especially for T44. The SLy5 force behaves better also in this system, in terms of convergence. The HF calculation easily lead to a triaxial minimum; Fig. 17 shows that with pairing force 1 (to which pairing gaps $\Delta_n = 0.7$
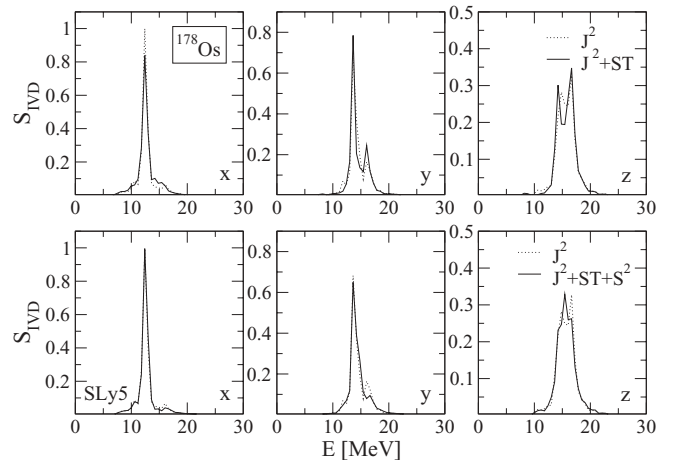

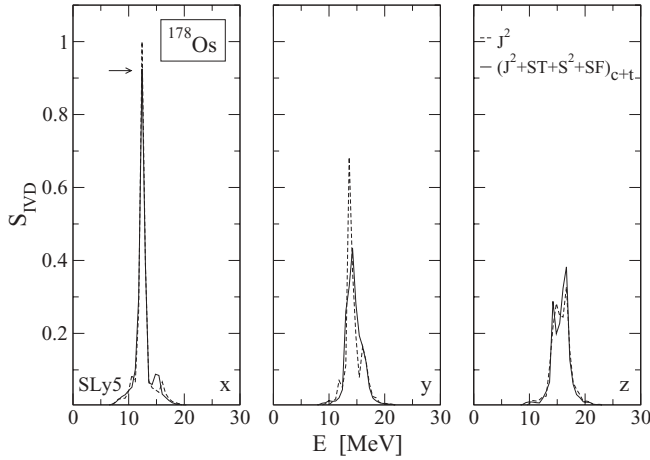FIG. 18. Same as Fig. 15 in ^{178}Os.

FIG. 19. Projection of the SLy5 IVD response along the three axes of ^{178}Os in the calculations explained in the main text in comparison to a purely central J^2 calculation. The arrow indicates the height of the main peak in the former calculation.

and $\Delta_p = 0.4$ MeV correspond), the γ parameter changes by ~13% when turning the spin-current terms on.

When performing TDHF calculations on top of the available mean-fields, we find outcomes similar to those of the triaxial case of ^{190}W (see Fig. 18): the central $S \cdot T$ contribution (three upper panels) provides an attractive effect on the y and z components and increases the spreading at variance with the S^2 terms (included in the three bottom panels). Along the main axis, with the $S \cdot T$ terms the signal relaxes down into the tails, which become fatter while the height of the main peak is reduced by ~18%. Figure 19 shows the comparison between a purely central J^2 calculation and the one including the tensor in a full way [except for the $(\nabla \cdot S)^2$ and $S \cdot \Delta S$ terms], with an evident difference in terms of fragmentation, especially on the y component (the total EWSR is still preserved). The instabilities associated to long time runs display rotational currents before the system expands itself in the whole model space.
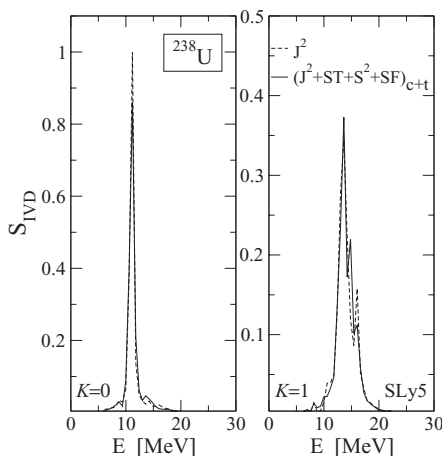

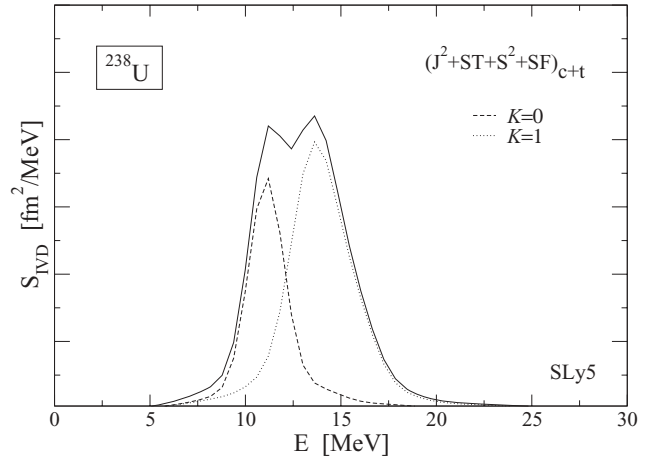FIG. 20. IVD components in ^{238}U for SLy5.

FIG. 21. IVD response in ^{238}U from SLy5 with the tensor contribution.

G. ^{238}U

The heaviest system considered in this work is the axially deformed ^{238}U ($\beta = 0.27$ with the SLy5 force). The inclusion of the tensor $S \cdot F$ contribution leads to a stable result, which is shown in Fig. 20 (solid line) in comparison to a simpler J^2 calculation (dashed line). The $K = 0$ and $K = 1$ modes are separately plotted in the left and right sides, respectively.

The resulting smoothed total strength distribution is shown in Fig. 21. The centroids of the $K = 0$ and $K = 1$ modes are located at 11.0 and 13.5 MeV, not far from the 10.92 and 13.98 MeV reported in Ref. [83].

After the smoothing, which simulates the broadening due to higher-order effects not accounted for in TDHF, the peaks just above 15 MeV are no longer resolved. Such a level of detail is dependent on the employed box (discretization) and other possible numerical artifacts. However, one cannot exclude that, when using different parameters, the full treatment of the tensor might more markedly affect the high-energy side of the strength distribution, which, in any case, appeared quite sensitive to the Skyrme set in calculations where the tensor was not included. For example, in Ref. [90], where a simpler functional based on the SkI3 set was employed, and in the separable RPA calculations of Ref. [91], based on the parameters from SLy6, a shoulder in that region was found. Finally, we recall that the modeling of higher-order correlations is expected to alter the tails of the strength function. Such extensions with the full Skyrme-tensor functional are undoubtedly envisaged for the future.

IV. CONCLUSIONS

This work presents the full implementation of the Skyrme energy density functional (EDF) complemented with the original formulation of the Skyrme-tensor force, in the three-dimensional time-dependent Hartree-Fock (3D-TDHF) with no symmetry restrictions. To our knowledge, this is the most complete development of TDHF concerning the p-h channel, where full self-consistency is achieved between Hartree-Fock and the dynamics (residual interaction) in the sense of no

suppression of terms. The derivation of the Skyrme-tensor Hartree-Fock energy is provided as an extension of Ref. [25].

The model has been applied in the linear limit, where the random-phase approximation (RPA) is recovered, to simulate the nuclear response in the 1^- channel, induced by the isovector dipole (IVD) operator. Comments about the methodology have been outlined and some self-consistency issues discussed.

Various benchmark nuclei with a mass number ranging from 16 to 238 have been considered and triaxial calculations have been presented. The overall results satisfy the empirical trend from the liquid drop model, although, as expected, deviations are found in the light region of mass, where the giant dipole resonance (GDR) energy is underestimated. More importantly, the gross features of the strength distribution from TDHF have been found in agreement with the experimental data or other theoretical works for all the systems where information are available.

The effects produced by each spin-dependent term of the p-h sector of the functional have been separately discussed. These are more visible for lighter nuclei where, in the RPA picture, fewer p-h configurations are involved in the response and Landau fragmentation is more pronounced. However, systematic outcomes are found for both the considered Skyrme forces (SLy5 and T44) from ^{16}O to ^{238}U: the GDR transition strength, which receives contributions from one-body transition densities (OBTDs) between parallel spin orbitals, is appreciably sensitive to the central spin-dependent part of the residual interaction. In particular, a behavior similar to calculations in other (charge-exchange) channels sensitive to the spin (-isospin) residual force has been noticed. This is the case of the Gamow-Teller resonance, modelled within a RPA formulated in the configuration space [60], the transition strength of which receives contributions from both spin-flip and non-spin-flip OBTDs. The S^2 terms tend to reinforce the residual interaction in the isovector channel, providing a repulsive effect on average and enhancing the strength of the resonance markedly in the considered cases. This dominant mechanism is countered by the $S \cdot T$ terms, which, although less important in the IVD channel than what was found in the (charge-exchange) 1^+ one, produces more fragmentation in the GR region.

On the recalled basis, one would conclude that the $S \cdot T$ terms, which are spin and velocity dependent, can be useful to balance the S^2 contribution of the current functionals. The former have been often suppressed in the past, together with their Galilean partners, the time-even $\overleftrightarrow{J}^2$ terms (cf. the discussion in Ref. [60] and Sec. II B). In Ref. [92], the removal of the $S \cdot T$ terms was found to improve the performance of the Skyrme EDF in infinite matter; however, as acknowledged by the same authors, this suppression would completely remove the $G_1^{T=0}$ and $G_1^{T=1}$ Landau parameters of the standard Skyrme functional, besides spoiling, with more or less manifested effects, the $G_0^{T=0}$, $G_0^{T=1}$ ones, which depend on both the t_0, t_3 and t_1, t_2 parameters respectively through the C_T^S and C_T^T coupling constants.

Besides influencing the spin-orbit splittings, the spin-current terms, associated to the pseudotensor $\overleftrightarrow{J}$, are of particular interest in connection to tensor studies, as they allow the tensor to become active even under time-reversal-invariant conditions. For this reason, they were the first tensor terms to be considered in the past [6], as well as more recently [7,55].

In the ground-state, the inclusion of the central $\overleftrightarrow{J}^2$ terms can markedly influence the deformation properties. In particular, variations of the deformation parameters up to $\sim$30–40% have been recorded in ^{28}Si, where the splitting between the $K = 0$, 1 modes accordingly changes by $\sim$1.5 MeV, and ^{178}Os. In ^{190}W, they turned out to drive the system to a triaxial shape.

The inclusion of the tensor at the $\overleftrightarrow{J}$ and $S \cdot T$ level does not introduce important changes on the IVD response in the considered cases. A small effect is produced by the $S \cdot F$ terms, but higher-precision calculations are required.

Particular attention has been paid to the pairing correlations, which affect the intrinsic deformation in terms of both the β and γ parameters. This has to be taken into consideration when discussing the predictive power of EDF-based calculations. More precisely, the impact of the smearing of the Fermi surface produced by a zero-range (monopole) pairing force has been discussed: different values of the pairing parameters have been considered, tuned against experimental masses, or exploited as additional degrees of freedom to force the intrinsic nuclear shape. The treatment of the p-p channel does not alter our conclusions about the p-h channel, where relative effects are mainly considered, and does not prevent a comparison with the experiment.

The occurrence of instabilities from the Skyrme functional has attracted particular interest in recent times (cf. Ref. [93] and references therein). In our calculations, various types of instabilities from the spin-density-dependent terms of the SLy5 or T44 functional have been found, which are enhanced in presence of derivatives, depend on the way the EDF terms couple one another and mix with the zero modes. They appear similarly to the possible cases described in Ref. [93]. This is especially true when the T44 force is employed, while the SLy5 set behaves more regularly. A peculiar case is represented by the performance of T44 in ^{24}Mg, where different truncations of the functional allow the spuriousities to dominate the scene in a relatively short time. This might be related to possible softness properties of this nucleus, which are predicted by some calculations [87]. The T44 force, moreover, turned out to hinder the convergence in the static Hartree-Fock quite easily in our calculations, making the numerics more difficult.

We notice that the S^2 and the $S \cdot T$ terms can produce an unphysical time-reversal breaking in both the ground-state and the long-term dynamics of the heavy γ-soft nuclei we considered. The inclusion of both those EDF contributions turned out to reduce the appearance of unwanted effects in some cases, with respect to the situation where only one of them is included. It similarly happens when the tensor is added to the central $S \cdot T$ terms, due to cancellations. The terms depending on the Laplacian and on the divergence of the spin density have not been analyzed in this work. No instabilities related to the Laplacian of the particle density or to the other time-even contributions have risen up, but more focused and systematic analyses in both sectors can be accomplished.

Unphysical dissipation effects in TDHF, when time-odd terms from the spin-orbit sector of the functional are suppressed, were observed in Ref. [36] and divergences taking place when running the simulation for a long time, in relation to couplings with zero modes, were mentioned in Ref. [20]. A more detailed study of such phenomena is envisaged also in view of computing the spin modes and we will deal with this subject in a separate work. The 3D-TDHF could represent a particularly sensitive testing tool for Skyrme(-like) energy density functionals in finite systems and complement information from infinite matter analyses [19,94]. Whereas the problem of instabilities might represent a limitation and demands a solution that does not drop terms, causing possible further spuriousities besides the lack of physical effects, useful information about the nuclear structure can be accessed through correlations associated to the symmetries breaking.

Changing the functional by dropping terms according to one's needs is useful for explorative purposes, the ultimate goal of this line of research still being the realization of a reliable functional, ideally flexible enough to adapt to disparate conditions. Finding the proper balance between the various spin-dependent terms would improve the predictive power of the current formulations. As is known, one conclusion of Ref. [7] was that the available parametrizations for the tensor force are not able to adjust the drawbacks of the central and spin-orbit part of the Skyrme functional, although it can offer extra degrees of freedom to fix the velocity-dependent terms. Interest is still driving the search for suitable constraints sensitive to the spin-dependent terms from excited states and/or ground-state properties. Clearly, in order to ensure predictability on collective excitations in the RPA or equivalent approaches that strongly depend on the underlying shell structure, coherent efforts are required to improve the description of the involved single-particle degrees of freedom.

The GDR energy is known to be correlated to the symmetry energy in dependence on the TRK enhancement factor, expressed in terms of the t_1 and t_2 parameters through the effective mass [95], which is already employed in fitting procedures (see, e.g., Ref. [67]). Input from the deformation splitting could also be taken into account.

Concerning further applications, we saw that the spin-dependent terms of the Skyrme functional can affect the tails of the nuclear response. The fraction of dipole strength concentrated in the low-energy tail of the GDR, around the threshold for particle emission, affects the photodisintegration rates, of particular interest for nucleosynthesis (see, e.g., Ref. [96]). In such a region, also pertaining to pygmy resonances, pairing correlations and the coupling to low-lying phonon can play a role [97]. The investigation of such an energy window by means of TDHF simulations, even in the linear approximation, is delicate, because proper attention is required to remove artifacts related to the Fourier transform and possible unphysical effects from the coupling to zero modes. In any case, the treatment of anharmonicities with the full Skyrme-tensor functional, in particular, the extensions to account for coupling to high-lying 2p-2h states, which is expected to be strengthened by the tensor force, would be an interesting step to undertake.

Finally, studying particle emission from collective excitations allows one to access information about the involved single-particle degrees of freedom as well as the mechanisms responsible for their cooperation, which is of interest for both the (interdependent) nuclear structure and nuclear interaction modeling.

APPENDIX A: THE UNRESTRICTED SKYRME-TENSOR HARTREE-FOCK ENERGY DENSITY FUNCTIONAL

In this Appendix, the derivation of the Skyrme energy density functional provided in Ref. [25] is extended in order to include the tensor contribution, under the general hypothesis of no symmetry restrictions. The original expression of the zero-range tensor force formulated by T. H. R. Skyrme [5] is used (the central and spin-orbit terms are not reported); for the sake of convenience, we rewrite it here as

$$
\begin{aligned}
v_\tau(1,2) = &\left\{ \frac{T}{2}[(\boldsymbol{\sigma}_1 \cdot \boldsymbol{k}')(\boldsymbol{\sigma}_2 \cdot \boldsymbol{k}')\delta(\boldsymbol{x}_1 - \boldsymbol{x}_2) + \delta(\boldsymbol{x}_1 - \boldsymbol{x}_2)(\boldsymbol{\sigma}_1 \cdot \boldsymbol{k})(\boldsymbol{\sigma}_2 \cdot \boldsymbol{k})] - \frac{T}{6}(\boldsymbol{\sigma}_1 \cdot \boldsymbol{\sigma}_2)[\boldsymbol{k}'^2\delta(\boldsymbol{x}_1 - \boldsymbol{x}_2) + \delta(\boldsymbol{x}_1 - \boldsymbol{x}_2)\boldsymbol{k}^2] \right. \\
&+ \frac{U}{2}[(\boldsymbol{\sigma}_1 \cdot \boldsymbol{k}')\delta(\boldsymbol{x}_1 - \boldsymbol{x}_2)(\boldsymbol{\sigma}_2 \cdot \boldsymbol{k}) + (\boldsymbol{\sigma}_1 \cdot \boldsymbol{k})\delta(\boldsymbol{x}_1 - \boldsymbol{x}_2)(\boldsymbol{\sigma}_2 \cdot \boldsymbol{k}')] \\
&\left. - \frac{U}{6}[(\boldsymbol{\sigma}_1 \cdot \boldsymbol{\sigma}_2)(\boldsymbol{k}' \cdot \delta(\boldsymbol{x}_1 - \boldsymbol{x}_2)\boldsymbol{k}) + (\boldsymbol{\sigma}_1 \cdot \boldsymbol{\sigma}_2)(\boldsymbol{k}'\delta(\boldsymbol{x}_1 - \boldsymbol{x}_2) \cdot \boldsymbol{k})] \right\} (1 - P_\sigma P_\tau P_M),
\end{aligned}
\tag{A1}
$$

where $\boldsymbol{k} = \frac{1}{2i}(\boldsymbol{\nabla}_1 - \boldsymbol{\nabla}_2)$ and $\boldsymbol{k}' = -\frac{1}{2i}(\boldsymbol{\nabla}'_1 - \boldsymbol{\nabla}'_2)$, respectively, act on the right and on the left, $\boldsymbol{\sigma}$ are the spin Pauli matrices, and P_σ, P_τ, P_M are the usual operators which exchange the spin, isospin, and spatial coordinates. When computing the Hartree-Fock energy (11), the $(1 - P_\sigma P_\tau P_M)$ operator allows, as for the Skyrme central and spin-orbit terms, to account for the exchange without antisymmetrizing the wave function in the ket. For the considered force, and under the hypothesis of no charge mixing, the product of the three exchange operators can be replaced by $\pm\delta_{q_1,q_2}$ ($q = p, n$) for the T- and U-weighted terms, respectively. To emphasize the spatial behavior of the corresponding interaction terms, the tensor parameters are defined as $T = 3t_e$ and $U = 3t_o$ in some works.

Although we deal with a zero-range force, it is appropriate to render the dependence on space more explicit in order to proceed with the calculation. By representing the σ_z diagonal basis by the set $\{|\omega\rangle\}$, where $\omega = 2m_s = \pm 1$ identifies the $\uparrow, \downarrow$ eigenvectors, the direct contribution to the Hartree-Fock energy from the first square brackets of Eq. (A1) is computed as

$$\triangle E_I^D = -\frac{T}{16} \sum_{i,j} \sum_{\omega_{1'},\omega_1,\omega_{2'}\omega_2} \int d\mathbf{R}\{\phi_i^*(\mathbf{x}_1', \omega_1')\phi_j^*(\mathbf{x}_2', \omega_2')\delta(\mathbf{x}_1 - \mathbf{x}_2)\delta(\mathbf{x}_1 - \mathbf{x}_1')\delta(\mathbf{x}_2 - \mathbf{x}_2')$$

$$[\langle\omega_1'|\boldsymbol{\sigma}_1|\omega_1\rangle \cdot (\boldsymbol{\nabla}_1 - \boldsymbol{\nabla}_2)][\langle\omega_2'|\boldsymbol{\sigma}_2|\omega_2\rangle \cdot (\boldsymbol{\nabla}_1 - \boldsymbol{\nabla}_2)]\phi_i(\mathbf{x}_1, \omega_1)\phi_j(\mathbf{x}_2, \omega_2)\} + \text{H.c.}, \tag{A2}$$

where H.c. denotes the Hermitian conjugate of what precedes and $d\mathbf{R}$ stands for $d\mathbf{x}_1'd\mathbf{x}_2'd\mathbf{x}_1d\mathbf{x}_2$ [in general, $\delta(\mathbf{x}_1 - \mathbf{x}_1')\delta(\mathbf{x}_2 - \mathbf{x}_2')$ ensures the force has a local character]. The subscripts i, j summarize the quantum numbers of the spinor $\psi_i(\mathbf{x}) = \sum_{\omega=\pm}\phi_i(\mathbf{x}, \omega)|\omega\rangle$; the isospin is represented through the charge q, among the other quantum numbers. In the following, unless differently specified, all the derivative operations apply to the right.

By inserting the definition of the spin-density (13) $\mathbf{S}_q(\mathbf{x}) = \mathbf{S}_q(\mathbf{x}, \mathbf{x}')|_{\mathbf{x}=\mathbf{x}'}$, where, like for the other densities, $\mathbf{S}(\mathbf{x}) = \sum_{q=p,n}\mathbf{S}_q(\mathbf{x})$ denotes the isoscalar density $\mathbf{S}_{T=0}(\mathbf{x})$, the previous energy contribution can be recast as

$$\triangle E_I^D = -\frac{T}{16} \sum_{\mu,\nu} \int d\mathbf{R}\{[2S_\nu(\mathbf{x}_2, \mathbf{x}_2')\nabla_{1,\mu}\nabla_{1,\nu}S_\mu(\mathbf{x}_1, \mathbf{x}_1') - \nabla_{1,\mu}S_\mu(\mathbf{x}_1, \mathbf{x}_1')\nabla_{2,\nu}S_\nu(\mathbf{x}_2, \mathbf{x}_2')$$

$$-\nabla_{1,\nu}S_\mu(\mathbf{x}_1, \mathbf{x}_1')\nabla_{2,\mu}S_\nu(\mathbf{x}_2, \mathbf{x}_2')] + \text{H.c.}\}_{\mathbf{x}_1=\mathbf{x}_1'=\mathbf{x}_2=\mathbf{x}_2'}. \tag{A3}$$

By inserting the relation (A.7) of Ref. [25]

$$\left[\nabla_\mu S_\nu^{(q)}(\mathbf{x}, \mathbf{x}')\right]_{\mathbf{x}=\mathbf{x}'} = \left[\nabla_\mu' S_\nu^{(q)}(\mathbf{x}, \mathbf{x}')\right]^*_{\mathbf{x}=\mathbf{x}'} = \tfrac{1}{2}\nabla_\mu S_\nu^{(q)}(\mathbf{x}) + i J_{\mu\nu}^{(q)}(\mathbf{x}) \tag{A4}$$

and the identity

$$\sum_{\mu\nu} S_\nu^{(q)}(\mathbf{x}_2, \mathbf{x}_2')(\nabla_{1',\mu}\nabla_{1',\nu} + \nabla_{1,\mu}\nabla_{1,\nu})S_\mu^{(q)}(\mathbf{x}_1, \mathbf{x}_1') = 2S_q(\mathbf{x}_2, \mathbf{x}_2') \cdot \mathbf{G}_q(\mathbf{x}_1, \mathbf{x}_1'), \tag{A5}$$

where $\mathbf{G}(\mathbf{x}) = \mathbf{G}(\mathbf{x}, \mathbf{x}')|_{\mathbf{x}=\mathbf{x}'}$ was introduced first in Eq. (18), the energy becomes

$$\triangle E_I^D = -\frac{T}{8} \int d\mathbf{x}_1 d\mathbf{x}_2 \left\{2\mathbf{S}(\mathbf{x}_1) \cdot \mathbf{G}(\mathbf{x}_2) - \frac{1}{4}[\boldsymbol{\nabla}_1 \cdot \mathbf{S}(\mathbf{x}_1)][\boldsymbol{\nabla}_2 \cdot \mathbf{S}(\mathbf{x}_2)] + J_0(\mathbf{x}_1)J_0(\mathbf{x}_2)\right.$$

$$\left. - \frac{1}{4}\sum_{\mu\nu}\nabla_{1,\mu}S_\nu(\mathbf{x}_1)\nabla_{2,\nu}S_\mu(\mathbf{x}_2) + \sum_{\mu\nu}J_{\mu\nu}(\mathbf{x}_1)J_{\nu\mu}(\mathbf{x}_2)\right\}_{\mathbf{x}_1=\mathbf{x}_2}. \tag{A6}$$

Performing integration by parts twice on the fourth term, after also the $\delta(\mathbf{x}_1 - \mathbf{x}_2)$ function has acted, and using, in each point of space, the identity

$$\sum_{\mu\nu} J_{\mu\nu}^{(q)} J_{\nu\mu}^{(q)} = \underline{J}_q^2 - \frac{1}{2}\mathbf{J}_q^2 + \frac{1}{3}\left(J_q^{(0)}\right)^2 \tag{A7}$$

for the last term, lead to

$$\triangle E_I^D = T \int d\mathbf{x}\left[-\frac{1}{4}\mathbf{S}(\mathbf{x}) \cdot \mathbf{G}(\mathbf{x}) + \frac{1}{16}(\boldsymbol{\nabla} \cdot \mathbf{S}(\mathbf{x}))^2 - \frac{1}{6}J_0^2(\mathbf{x}) - \frac{1}{8}\underline{J}^2(\mathbf{x}) + \frac{1}{16}\mathbf{J}^2(\mathbf{x})\right]. \tag{A8}$$

By similarly proceeding for the remnant terms of the tensor force that are weighted by the parameter T, one gets

$$\triangle E_{II}^D = \frac{T}{24} \sum_{\mu,\nu} \int d\mathbf{R}\{[S_\nu(\mathbf{x}_2, \mathbf{x}_2')(\nabla_{1,\mu})^2 S_\nu(\mathbf{x}_1, \mathbf{x}_1') - \nabla_{2,\mu}S_\nu(\mathbf{x}_2, \mathbf{x}_2')\nabla_{1,\mu}S_\nu(\mathbf{x}_1, \mathbf{x}_1')] + \text{H.c.}\}_{\mathbf{x}_1=\mathbf{x}_1'=\mathbf{x}_2=\mathbf{x}_2'}.$$

By using the relation (A.6) of Ref. [25]

$$[(\nabla^2 + \nabla'^2)S_\mu^{(q)}(\mathbf{x}, \mathbf{x}')]_{\mathbf{x}=\mathbf{x}'} = \triangle S_\mu^{(q)}(\mathbf{x}) - 2T_\mu^{(q)}(\mathbf{x}), \tag{A9}$$

in addition to Eq. (A4), one obtains

$$\triangle E_{II}^D = \frac{T}{24} \int d\mathbf{x}_1 d\mathbf{x}_2 \left\{\mathbf{S}(\mathbf{x}_2) \cdot \triangle\mathbf{S}(\mathbf{x}_1) - 2\mathbf{S}(\mathbf{x}_2) \cdot \mathbf{T}(\mathbf{x}_1) - \frac{1}{2}\nabla_{2,\mu}S_\nu(\mathbf{x}_2)\nabla_{1,\mu}S_\nu(\mathbf{x}_1) + 2\sum_{\mu\nu}J_{\mu\nu}(\mathbf{x}_2)J_{\mu\nu}(\mathbf{x}_1)\right\}_{\mathbf{x}_1=\mathbf{x}_2}.$$

Once again, due to the zero-range nature of the interaction, after one single integration by parts on the next-to-last term, one has

$$\triangle E_{\mathrm{II}}^D = T \int d\boldsymbol{x} \left[\frac{1}{16} \boldsymbol{S}(\boldsymbol{x}) \cdot \triangle \boldsymbol{S}(\boldsymbol{x}) - \frac{1}{12} \boldsymbol{S}(\boldsymbol{x}) \cdot \boldsymbol{T}(\boldsymbol{x}) + \frac{1}{12} \overset{\leftrightarrow}{J}^2(\boldsymbol{x}) \right] ; \tag{A10}$$

the square of the tensor of rank two $\overset{\leftrightarrow}{J}$ is defined, as usual, by $\overset{\leftrightarrow}{J}_q^2 = \sum_{\mu\nu} (J_{\mu\nu}^{(q)})^2$ and, for every point $\boldsymbol{x}$, the relation

$$\overset{\leftrightarrow}{J}_q^2 = \underline{J}_q^2 + \tfrac{1}{2} \boldsymbol{J}_q^2 + \tfrac{1}{3} \left(J_q^{(0)} \right)^2 \tag{A11}$$

holds. By summing up the two energies $\triangle E_{\mathrm{I}}^D$ and $\triangle E_{\mathrm{II}}^D$ and taking into account the exchange, the total T-weighted contribution to the tensor energy is

$$
\begin{aligned}
&\triangle E_T^{D+E} \\
&= \frac{T}{4} \int d\boldsymbol{x} \Bigg(\left\{ \frac{1}{4} \boldsymbol{S}(\boldsymbol{x}) \cdot \triangle \boldsymbol{S}(\boldsymbol{x}) - \frac{1}{3} \boldsymbol{S}(\boldsymbol{x}) \cdot \boldsymbol{T}(\boldsymbol{x}) + \frac{3}{4} [\nabla \cdot \boldsymbol{S}(\boldsymbol{x})]^2 + \boldsymbol{S}(\boldsymbol{x}) \cdot \boldsymbol{F}(\boldsymbol{x}) - \frac{5}{9} J_0^2(\boldsymbol{x}) + \frac{5}{12} \boldsymbol{J}^2(\boldsymbol{x}) - \frac{1}{6} \underline{J}^2(\boldsymbol{x}) \right\} \\
&\quad - \sum_{q=p,n} \left\{ \frac{1}{4} \boldsymbol{S}_q(\boldsymbol{x}) \cdot \triangle \boldsymbol{S}_q(\boldsymbol{x}) - \frac{1}{3} \boldsymbol{S}_q(\boldsymbol{x}) \cdot \boldsymbol{T}_q(\boldsymbol{x}) + \frac{3}{4} [\nabla \cdot \boldsymbol{S}_q(\boldsymbol{x})]^2 + \boldsymbol{S}_q(\boldsymbol{x}) \cdot \boldsymbol{F}_q(\boldsymbol{x}) - \frac{5}{9} \left(J_q^{(0)} \right)^2(\boldsymbol{x}) + \frac{5}{12} \boldsymbol{J}_q^2(\boldsymbol{x}) - \frac{1}{6} \underline{J}_q^2(\boldsymbol{x}) \right\} \Bigg),
\end{aligned}
\tag{A12}
$$

where our equation

$$- \int (\nabla \cdot \boldsymbol{S}(\boldsymbol{x}))^2 d\boldsymbol{x} = 2 \int [\boldsymbol{S}(\boldsymbol{x}) \cdot \boldsymbol{G}(\boldsymbol{x}) + \boldsymbol{S}(\boldsymbol{x}) \cdot \boldsymbol{F}(\boldsymbol{x})] d\boldsymbol{x} \tag{A13}$$

has been used. As a matter of fact, the integration by parts of the square of the divergence of the spin density reads (the integral will be omitted)

$$
\begin{aligned}
(\nabla \cdot \boldsymbol{S}(\boldsymbol{x}))^2 &= \sum_{\mu\nu} \nabla_\mu S_\mu(\boldsymbol{x}) \nabla_\nu S_\nu(\boldsymbol{x}) = - \sum_{\mu\nu} S_\mu(\boldsymbol{x}_2, \boldsymbol{x}_2') [\nabla_{1',\mu} \nabla_{1,\nu} S_\nu(\boldsymbol{x}_1, \boldsymbol{x}_1') + \nabla_{1,\mu} \nabla_{1,\nu} S_\nu(\boldsymbol{x}_1, \boldsymbol{x}_1') \\
&\quad + \nabla_{1',\mu} \nabla_{1',\nu} S_\nu(\boldsymbol{x}_1, \boldsymbol{x}_1') + \nabla_{1',\mu} \nabla_{1,\nu} S_\nu(\boldsymbol{x}_1, \boldsymbol{x}_1')]_{\boldsymbol{x}_1 = \boldsymbol{x}_1' = \boldsymbol{x}_2 = \boldsymbol{x}_2'}
\end{aligned}
\tag{A14}
$$

and one can recognize the structure of the $\boldsymbol{S} \cdot \boldsymbol{F}$ and $\boldsymbol{S} \cdot \boldsymbol{G}$ terms on the right.

Concerning the terms weighted by the U coefficient, the contribution from the first addend in Eq. (A1) reads

$$
\begin{aligned}
\triangle E_{\mathrm{III}}^D &= \frac{U}{16} \sum_{i,j} \sum_{\omega_{1'},\omega_1,\omega_{2'},\omega_2} \sum_{\mu\nu} \int d\boldsymbol{R} \big\{ \big[\Psi_i^{*(\mu)}(\boldsymbol{x}_1', \omega_1') \phi_j^*(\boldsymbol{x}_2', \omega_2') - \phi_i(\boldsymbol{x}_1', \omega_1') \Psi_j^{*(\mu)}(\boldsymbol{x}_2', \omega_2') \big] \\
&\quad \sigma_\mu^{(1)} \delta \sigma_\nu^{(2)} \big[\Psi_i^{(\nu)}(\boldsymbol{x}_1, \omega_1) \phi_j(\boldsymbol{x}_2, \omega_2) - \phi_i(\boldsymbol{x}_1, \omega_1) \Psi_j^{(\nu)}(\boldsymbol{x}_2, \omega_2) \big] \big\},
\end{aligned}
\tag{A15}
$$

where the definition $\Psi_\mu(\boldsymbol{y}, \omega) = [\nabla_\mu \phi(\boldsymbol{x}, \omega)]_{\boldsymbol{x}=\boldsymbol{y}}$ and the short-hand notation $\delta = \delta(\boldsymbol{x}_1 - \boldsymbol{x}_2) \delta(\boldsymbol{x}_1 - \boldsymbol{x}_1') \delta(\boldsymbol{x}_2 - \boldsymbol{x}_2')$ have been introduced. By inserting the definition of the spin density, after a few algebric steps one obtains

$$
\begin{aligned}
\triangle E_{\mathrm{III}}^D &= \frac{U}{16} \sum_{\mu\nu} \int d\boldsymbol{R} \{ S_\nu(\boldsymbol{x}_2, \boldsymbol{x}_2') \nabla_{1',\mu} \nabla_{1,\nu} S_\mu(\boldsymbol{x}_1, \boldsymbol{x}_1') - \nabla_{1',\mu} S_\mu(\boldsymbol{x}_1, \boldsymbol{x}_1') \nabla_{2,\nu} S_\nu(\boldsymbol{x}_2, \boldsymbol{x}_2') \\
&\quad - \nabla_{1,\nu} S_\mu(\boldsymbol{x}_1, \boldsymbol{x}_1') \nabla_{2',\mu} S_\nu(\boldsymbol{x}_2, \boldsymbol{x}_2') + S_\mu(\boldsymbol{x}_1, \boldsymbol{x}_1') \nabla_{2,\nu} \nabla_{2',\mu} S_\nu(\boldsymbol{x}_2, \boldsymbol{x}_2') \}_{\boldsymbol{x}_1 = \boldsymbol{x}_1' = \boldsymbol{x}_2 = \boldsymbol{x}_2'}.
\end{aligned}
\tag{A16}
$$

By using the relation (A4) and the identity

$$\sum_{\mu\nu} S_\nu^{(q)}(\boldsymbol{x}_2, \boldsymbol{x}_2') (\nabla_{1,\mu}' \nabla_{1,\nu} + \nabla_{1,\mu} \nabla_{1,\nu}') S_\mu^{(q)}(\boldsymbol{x}_1, \boldsymbol{x}_1') = 2 \boldsymbol{S}_q(\boldsymbol{x}_2, \boldsymbol{x}_2') \cdot \boldsymbol{F}_q(\boldsymbol{x}_1, \boldsymbol{x}_1'), \tag{A17}$$

after having renamed $\boldsymbol{x}_1 \leftrightarrow \boldsymbol{x}_2$, $\boldsymbol{x}_1' \leftrightarrow \boldsymbol{x}_2'$ and $\mu \leftrightarrow \nu$ in the fourth term, one is led to

$$
\begin{aligned}
\triangle E_{\mathrm{III}}^D &= \frac{U}{16} \int d\boldsymbol{x}_1 d\boldsymbol{x}_2 \Bigg\{ 2\boldsymbol{S}(\boldsymbol{x}_2) \cdot \boldsymbol{F}(\boldsymbol{x}_1) - \frac{1}{4} [\nabla_1 \cdot \boldsymbol{S}(\boldsymbol{x}_1)][\nabla_2 \cdot \boldsymbol{S}(\boldsymbol{x}_2)] - J_0(\boldsymbol{x}_1) J_0(\boldsymbol{x}_2) \\
&\quad - \frac{1}{4} \sum_{\mu\nu} \nabla_{1,\nu} S_\mu(\boldsymbol{x}_1) \nabla_{2,\mu} S_\nu(\boldsymbol{x}_2) - \sum_{\mu\nu} J_{\nu\mu}(\boldsymbol{x}_1) J_{\mu\nu}(\boldsymbol{x}_2) \Bigg\}_{\boldsymbol{x}_1 = \boldsymbol{x}_2}.
\end{aligned}
\tag{A18}
$$

The corresponding H.c. term in Eq. (A1), treated in the same way, provides an identical integral and one can multiply the previous result by a factor 2. By performing the same steps used to obtain Eq. (A8) we get

$$\triangle E_{\text{III}}^{D} = \frac{U}{8} \int dx \left[2S(x) \cdot F(x) - \frac{1}{2}(\nabla \cdot S(x))^2 - J_0{}^2(x) - \sum_{\mu\nu} J_{\mu\nu}(x) J_{\nu\mu}(x) \right] \tag{A19}$$

and, thus,

$$\triangle E_{\text{III}}^{D} = \frac{U}{8} \int dx \left[2S(x) \cdot F(x) - \frac{1}{2}(\nabla \cdot S(x))^2 - \frac{4}{3} J_0{}^2(x) + \frac{1}{2} J^2(x) - \underline{J}^2(x) \right]. \tag{A20}$$

For the last line of Eq. (A1), the different spin-momentum structure allows a simpler expression,

$$\triangle E_{\text{IV}}^{D} = -\frac{U}{24} \sum_{i,j} \sum_{\omega_{1'},\omega_1,\omega_{2'},\omega_2} \sum_{\mu} \int dR \{ [\Psi_i^{*(\mu)}(x_1', \omega_1')\phi_j^*(x_2', \omega_2') - \phi_i^*(x_1', \omega_1')\Psi_j^{*(\mu)}(x_2', \omega_2')]$$

$$\sigma_1 \cdot \sigma_2 \delta [\Psi_i^{(\mu)}(x_1, \omega_1)\phi_j(x_2, \omega_2) - \phi_i(x_1, \omega_1)\Psi_j^{(\mu)}(x_2, \omega_2)] \}, \tag{A21}$$

equal to

$$\triangle E_{\text{IV}}^{D} = -\frac{U}{12} \int dR \sum_{\mu\nu} \{ S_\nu(x_2, x_2')\nabla_{1',\mu}\nabla_{1,\mu} S_\nu(x_1, x_1') - \nabla_{1',\mu} S_\nu(x_1, x_1')\nabla_{2,\mu} S_\nu(x_2, x_2') \}_{x_1 = x_1' = x_2 = x_2'}. \tag{A22}$$

By using the relations (A4) one more time and recognizing the scalar product between the spin and the kinetic density

$$\sum_{\mu} S_\mu^{(q)}(x_2, x_2')\nabla_{1'} \cdot \nabla_1 S_\mu^{(q)}(x_1, x_1') = S_q(x_2, x_2') \cdot T_q(x_1, x_1') \tag{A23}$$

one obtains

$$\triangle E_{\text{IV}}^{D} = -\frac{U}{12} \int dx_1 dx_2 \left\{ S(x_2) \cdot T(x_1) - \frac{1}{4} \sum_{\mu\nu} \nabla_{2,\mu} S_\nu(x_2)\nabla_{1,\mu} S_\nu(x_1) - \sum_{\mu\nu} J_{\mu\nu}(x_1) J_{\mu\nu}(x_2) \right\}_{x_1 = x_2},$$

that is,

$$\triangle E_{\text{IV}}^{D} = -\frac{U}{12} \int dx \left[S(x) \cdot T(x) + \frac{1}{4} S(x) \cdot \triangle S(x) - \overleftrightarrow{J}^2(x) \right]. \tag{A24}$$

By adding together $\triangle E_{\text{III}}^{D}$ and $\triangle E_{\text{IV}}^{D}$, the final result is

$$\triangle E_U^D = \int dx \frac{U}{12} \left[3S(x) \cdot F(x) - S(x) \cdot T(x) - \frac{1}{4} S(x)\triangle S(x) - \frac{3}{4}(\nabla \cdot S)^2(x) - \frac{5}{3} J_0{}^2(x) + \frac{5}{4} J^2(x) - \frac{1}{2}\underline{J}^2(x) \right]. \tag{A25}$$

The direct plus exchange provides

$$\triangle E_U^{D+E}$$

$$= \frac{U}{12} \int dx \left\{ 3S(x) \cdot F(x) - S(x) \cdot T(x) - \frac{1}{4} S(x) \cdot \triangle S(x) - \frac{3}{4}(\nabla \cdot S)^2(x) - \frac{5}{3} J_0{}^2(x) + \frac{5}{4} J^2(x) - \frac{1}{2}\underline{J}^2(x) \right.$$

$$\left. + \sum_{q=p,n} \left[3S_q(x) \cdot F_q(x) - S_q(x) \cdot T_q(x) - \frac{1}{4} S_q(x) \cdot \triangle S_q(x) - \frac{3}{4}(\nabla \cdot S_q)^2(x) - \frac{5}{3}(J_q^{(0)})^2(x) + \frac{5}{4} J_q^2(x) - \frac{1}{2}\underline{J}_q^2(x) \right] \right\}. \tag{A26}$$

The sum of the integrand in Eqs. (A12) and (A26) provides the tensor contribution to the standard Skyrme energy density functional, denoted by $\mathcal{H}_{\text{tens}}$ in Eq. (16).

By defining as D_α (E_α) the weight of a generic term α belonging to the direct (exchange) contributions to the energy, the relations $D_\alpha = C_0^\alpha - C_1^\alpha$ and $D_\alpha + E_\alpha = C_0^\alpha + C_1^\alpha$ hold, where $C_{T=0,1}^\alpha$ are the isoscalar and isovector coupling constants employed in some other works. By rearranging the result in terms of the isoscalar and isovector densities,

the sum of the expressions (49a) + (49b) of Ref. [58] is recovered. Otherwise, when the $S \cdot G$ terms from Eq. (A8) are retained, the $S \cdot F$ and $(\nabla \cdot S)^2$ coupling constants in (A12) change according to the combination (a) of Table IX; in such a way, one obtains, in the proton-neutron formalism, the more general formulation of Eq. (16), where $A_\alpha = D_\alpha + E_\alpha$ and $B_\alpha = D_\alpha$. Since $E_\alpha = \mp D_\alpha$ for the $T(-)$ and $U(+)$ contributions, only the U-weighted terms contribute to A_α.

TABLE IX. Two possible combinations of the D_α coupling constants for the direct functional's terms listed in the first row. Set (a) corresponds to what is straightforwardly obtained for the direct contributions through the derivation presented here, when Eq. (A13) is not used. Set (b), on which the result (A12) is based, leads to recovery of the expression of Ref. [58]. In both cases, the Galilean invariance of the functional is fulfilled [see Eqs. (29)].

Set	$\mathbf{S} \cdot \mathbf{G}$	$\mathbf{S} \cdot \mathbf{F}$	$(\mathbf{\nabla} \cdot \mathbf{S})^2$
(a)	$\frac{T}{4}$	$\frac{U}{4}$	$\frac{1}{16}(T - U)$
(b)	0	$\frac{1}{4}(T + U)$	$\frac{1}{16}(3T - U)$

APPENDIX B: DENSITIES AND CURRENTS OF THE SKYRME-TENSOR EDF

In this Appendix, the expressions of the densities and currents entering the Skyrme energy density functional (16) are provided. For the sake of simplicity, we take as implicit the sum over the wave-functions index, which includes all the quantum numbers with the exception of the spin projection ω, which is separately written.

When boosting the Hartree-Fock single particles, they gain an imaginary part. We adopt the definitions of Table X, where $\phi_\omega = \phi(\mathbf{x}, \omega)$, $k = x, y, z$, and $\omega = 2m_s = \pm 1$, and of Table XI, where the second-order terms are listed. In the following, all the relations hold if considering isoscalar, isovector, neutron, or proton densities.

The densities which are even under the time-reversal operation $T_K : \phi_i(\mathbf{x}, \omega) \to -\omega \phi^*(\mathbf{x}, -\omega)$ ($T_K = -i\sigma_y K_0$, where K_0 denotes the complex conjugation) include

(i) the particle density

$$\rho(\mathbf{x}) = \sum_\omega \phi^*(\mathbf{x}', \omega)\phi(\mathbf{x}, \omega)|_{\mathbf{x}=\mathbf{x}'} \quad \text{(B1)}$$

$$= \sum_\omega \left[(\phi_\omega^R)^2 + (\phi_\omega^I)^2 \right] = \sum_\omega |\phi_\omega|^2; \quad \text{(B2)}$$

(ii) the kinetic density

$$\tau(\mathbf{x}) = [\mathbf{\nabla} \cdot \mathbf{\nabla}' \rho(\mathbf{x}, \mathbf{x}')]_{\mathbf{x}=\mathbf{x}'} \quad \text{(B3)}$$

$$= \sum_\omega \left[(\mathbf{\nabla}\phi_\omega^R)^2 + (\mathbf{\nabla}\phi_\omega^I)^2 \right] = \sum_\omega |\mathbf{\Psi}_\omega|^2; \quad \text{(B4)}$$

(iii) the spin-current pseudotensor $\overset{\leftrightarrow}{J}$

$$\overset{\leftrightarrow}{J}(\mathbf{x}) = \frac{1}{2i}[(\mathbf{\nabla} - \mathbf{\nabla}') \otimes \mathbf{S}(\mathbf{x}, \mathbf{x}')]_{\mathbf{x}=\mathbf{x}'}. \quad \text{(B5)}$$

TABLE X. Conventions (I) adopted in the current Appendix.

ϕ_ω^R	$\mathrm{Re}\,\phi_\omega$
ϕ_ω^I	$\mathrm{Im}\,\phi_\omega$
Ψ_k^ω	$\nabla_k \phi_\omega$
$\tilde{\Psi}_k^\omega$	$\nabla_k \phi_\omega^*$
$\mathbf{\Psi}_\omega$	$\nabla \phi_\omega$
$\tilde{\mathbf{\Psi}}_\omega$	$\nabla \phi_\omega^*$
$\Psi_k^{R,\omega}$	$\mathrm{Re}\,\Psi_k^\omega$
$\Psi_k^{I,\omega}$	$\mathrm{Im}\,\Psi_k^\omega$
$\mathbf{\Psi}_\omega^{R(I)}$	$\mathrm{Re(Im)}\,\mathbf{\Psi}_\omega$

TABLE XI. Conventions (II) adopted in the current appendix.

$\Psi_{kk'}^\omega$	$\nabla_k \nabla_{k'} \phi_\omega$
$\tilde{\Psi}_{kk'}^\omega$	$\nabla_k \nabla_{k'} \phi_\omega^*$
$\Psi_{kk'}^{R,\omega}$	$\mathrm{Re}\,\Psi_{k,k'}^\omega$
$\Psi_{kk'}^{I,\omega}$	$\mathrm{Im}\,\Psi_{k,k'}^\omega$

The nine components ($k = x, y, z$) can be implemented as

$$J_{kx} = \sum_{\omega,\omega'=\pm 1, \omega \neq \omega'} \left[\phi_\omega^R \Psi_k^{I,\omega'} - \phi_\omega^I \Psi_k^{R,\omega'} \right]$$

$$= +\mathrm{Im}[\phi_+^* \Psi_k^- + \phi_-^* \Psi_k^+] \quad \text{(B6)}$$

$$J_{ky} = \sum_{L=R,I} [\phi_-^L \Psi_k^{L,+} - \phi_+^L \Psi_k^{L,-}]$$

$$= -\mathrm{Re}[\phi_+^* \Psi_k^- - \phi_-^* \Psi_k^+] \quad \text{(B7)}$$

$$J_{kz} = \phi_+^R \Psi_k^{I,+} - \phi_+^I \Psi_k^{R,+} + \phi_-^I \Psi_k^{R,-} - \phi_-^R \Psi_k^{I,-}$$

$$= +\mathrm{Im}[\phi_+^* \Psi_k^+ - \phi_-^* \Psi_k^-]. \quad \text{(B8)}$$

The time-odd densities are

(i) the spin density

$$\mathbf{S}(\mathbf{x}) = \sum_{\omega,\omega'} \phi^*(\mathbf{x}', \omega')\phi(\mathbf{x}, \omega)\langle \omega' | \boldsymbol{\sigma} | \omega \rangle \big|_{\mathbf{x}=\mathbf{x}'}, \quad \text{(B9)}$$

where each component corresponds to

$$S_x = 2[\phi_+^R \phi_-^R + \phi_+^I \phi_-^I] = 2\mathrm{Re}[\phi_+^* \phi_-] \quad \text{(B10)}$$

$$S_y = 2[\phi_+^R \phi_-^I - \phi_-^R \phi_+^I] = 2\mathrm{Im}[\phi_+^* \phi_-] \quad \text{(B11)}$$

$$S_z = \sum_{L=R,I} [\phi_+^L \phi_+^L - \phi_-^L \phi_-^L] = \mathrm{Re}[\phi_+^* \phi_+ - \phi_-^* \phi_-] \quad \text{(B12)}$$

(ii) the momentum density

$$\mathbf{j}(\mathbf{x}) = -\frac{i}{2}[(\mathbf{\nabla} - \mathbf{\nabla}')\rho(\mathbf{x}, \mathbf{x}')]_{\mathbf{x}=\mathbf{x}'}, \quad \text{(B13)}$$

with components equal to

$$j_k = \sum_{\omega=\pm} \left[\phi_\omega^R \Psi_x^{I,\omega} - \phi_\omega^I \Psi_x^{R,\omega} \right]$$

$$= \mathrm{Im}[\phi_+^* \Psi_x^+ + \phi_-^* \Psi_x^-]; \quad \text{(B14)}$$

(iii) the spin kinetic density

$$\mathbf{T}(\mathbf{x}) = [\mathbf{\nabla} \cdot \mathbf{\nabla}' \mathbf{S}(\mathbf{x}, \mathbf{x}')]_{\mathbf{x}=\mathbf{x}'}, \quad \text{(B15)}$$

where

$$T_x = 2[\mathbf{\Psi}_+^R \mathbf{\Psi}_-^R + \mathbf{\Psi}_+^I \mathbf{\Psi}_-^I]$$

$$= 2\mathrm{Re}[\mathbf{\Psi}_- \tilde{\mathbf{\Psi}}_+] \quad \text{(B16)}$$

$$T_y = 2[\mathbf{\Psi}_+^R \mathbf{\Psi}_-^I - \mathbf{\Psi}_+^I \mathbf{\Psi}_-^R]$$

$$= 2\mathrm{Im}[\mathbf{\Psi}_- \tilde{\mathbf{\Psi}}_+] \quad \text{(B17)}$$

$$T_z = \sum_{L=R,I} [\mathbf{\Psi}_+^L \mathbf{\Psi}_+^L - \mathbf{\Psi}_-^L \mathbf{\Psi}_-^L]$$

$$= \mathrm{Re}[\mathbf{\Psi}_+ \tilde{\mathbf{\Psi}}_+ - \mathbf{\Psi}_- \tilde{\mathbf{\Psi}}_-]; \quad \text{(B18)}$$

(iv) the pseudovector $\boldsymbol{F}(\boldsymbol{x})$ density

$$\boldsymbol{F}(\boldsymbol{x}) = \tfrac{1}{2}\left\{\left[(\nabla'\otimes\nabla) + (\nabla\otimes\nabla')\right]\boldsymbol{S}(\boldsymbol{x},\boldsymbol{x}')\right\}_{\boldsymbol{x}=\boldsymbol{x}'}.$$

It can be conveniently represented by splitting each k component in three contributions

$$F_k(\boldsymbol{x}) = \sum_{k'=x,y,z} F_k^{(k')}(\boldsymbol{x}), \tag{B19}$$

where the single terms read

$$F_x^{(x)} = 2\left[\Psi_x^{R,+}\Psi_x^{R,-} + \Psi_x^{I,+}\Psi_x^{I,-}\right]$$
$$= 2\mathrm{Re}[\tilde{\Psi}_x^+\Psi_x^-] \tag{B20}$$

$$F_x^{(y)} = \sum_{k,k'=x,y;k\neq k'}\left[\Psi_k^{I,-}\Psi_{k'}^{R,+} - \Psi_{k'}^{I,+}\Psi_k^{R,-}\right]$$
$$= \mathrm{Im}[\tilde{\Psi}_x^+\Psi_y^- - \tilde{\Psi}_x^-\Psi_y^+] \tag{B21}$$

$$F_x^{(z)} = \sum_{L=R,I}\left[\Psi_x^{L,+}\Psi_z^{L,+} - \Psi_x^{L,-}\Psi_z^{L,-}\right]$$
$$= \mathrm{Re}[\tilde{\Psi}_x^+\Psi_z^+ - \tilde{\Psi}_x^-\Psi_z^-] \tag{B22}$$

$$F_y^{(x)} = \sum_{L=R,I}\left[\Psi_y^{L,+}\Psi_x^{L,-} + \Psi_y^{L,-}\Psi_x^{L,+}\right]$$
$$= \mathrm{Re}[\tilde{\Psi}_y^+\Psi_x^- + \tilde{\Psi}_y^-\Psi_x^+] \tag{B23}$$

$$F_y^{(y)} = 2\left[\Psi_y^{I,-}\Psi_y^{R,+} - \Psi_y^{R,-}\Psi_y^{I,+}\right]$$
$$= -2\mathrm{Im}[\tilde{\Psi}_y^-\Psi_y^+] \tag{B24}$$

$$F_y^{(z)} = F_x^{(z)}\big|_{x\to y} \tag{B25}$$

$$F_z^{(x)} = F_y^{(x)}\big|_{y\to z} \tag{B26}$$

$$F_z^{(y)} = F_x^{(y)}\big|_{x\to z} \tag{B27}$$

$$F_z^{(z)} = \sum_{L=R,I}\left[(\Psi_z^{L,+})^2 - (\Psi_z^{L,-})^2\right]$$
$$= \mathrm{Re}[\tilde{\Psi}_z^+\Psi_z^+ - \tilde{\Psi}_z^-\Psi_z^-]; \tag{B28}$$

(v) the pseudovector $\boldsymbol{G}(\boldsymbol{x})$ density

$$\boldsymbol{G}(\boldsymbol{x}) = \tfrac{1}{2}\{[(\nabla'\otimes\nabla') + (\nabla\otimes\nabla)]\boldsymbol{S}(\boldsymbol{x},\boldsymbol{x}')\}_{\boldsymbol{x}=\boldsymbol{x}'};$$

by proceeding similarly to $\boldsymbol{F}(\boldsymbol{x})$, we obtain

$$G_x^{(x)} = \sum_{L=R,I}[\phi_+^L \triangle_x \phi_-^L + \phi_-^L \triangle_x \phi_+^L]$$
$$= \mathrm{Re}[\phi_+^* \triangle_x \phi_- + \phi_-^* \triangle_x \phi_+] \tag{B29}$$

$$G_x^{(y)} = \phi_+^R\Psi_{xy}^{I,-} - \phi_+^I\Psi_{xy}^{R,-} + \phi_-^I\Psi_{xy}^{R,+} - \phi_-^R\Psi_{xy}^{I,+}$$
$$= \mathrm{Im}[\phi_+^*\Psi_{xy}^- - \phi_-^*\Psi_{xy}^+] \tag{B30}$$

$$G_x^{(z)} = \sum_{L=R,I}\left[\phi_+^L\Psi_{xz}^{L,+} - \phi_-^L\Psi_{xz}^{L,-}\right]$$
$$= \mathrm{Re}[\phi_+^*\Psi_{xz}^+ - \phi_-^*\Psi_{xz}^-] \tag{B31}$$

$$G_y^{(x)} = \sum_{L=R,I}\left[\phi_+^L\Psi_{yx}^{L,-} + \phi_-^L\Psi_{yx}^{L,+}\right]$$
$$= \mathrm{Re}[\phi_+^*\Psi_{yx}^- + \phi_-^*\Psi_{yx}^+] \tag{B32}$$

$$G_y^{(y)} = \phi_-^R \triangle_y \phi_-^I - \phi_+^I \triangle_y \phi_-^R$$
$$\quad + \phi_-^I \triangle_y \phi_+^R - \phi_-^R \triangle_y \phi_+^I$$
$$= \mathrm{Im}[\phi_+^* \triangle_y \phi_- - \phi_-^* \triangle_y \phi_+] \tag{B33}$$

$$G_y^{(z)} = G_x^{(z)}\big|_{x\to y} \tag{B34}$$

$$G_z^{(x)} = G_y^{(x)}\big|_{y\to z} \tag{B35}$$

$$G_z^{(y)} = G_x^{(y)}\big|_{x\to z} \tag{B36}$$

$$G_z^{(z)} = \sum_{L=R,I}[\phi_+^L \triangle_z \phi_+^L - \phi_-^L \triangle_z \phi_-^L]$$
$$= \mathrm{Re}[\phi_+^* \triangle_z \phi_+ - \phi_-^* \triangle_z \phi_-]. \tag{B37}$$

---

[1] D. J. Rowe, *Nuclear Collective Motion* (Methuen & Co., London, 1970); P. Ring and P. Schuck, *The Nuclear Many-Body Problem* (Springer-Verlag, New York, 1980).

[2] P. D. Stevenson, E. B. Suckling, S. Fracasso, and A. S. Umar (to be published).

[3] E. B. Suckling, Ph.D. thesis, University of Surrey, 2011.

[4] Y. Iwata and J. A. Maruhn, Phys. Rev. C **84**, 014616 (2011).

[5] T. H. R. Skyrme, Nucl. Phys. **9**, 615 (1959).

[6] Fl. Stancu, D. M. Brink, and H. Flocard, Phys. Lett. B **68**, 108 (1977).

[7] T. Lesinski, M. Bender, K. Bennaceur, T. Duguet, and J. Meyer, Phys. Rev. C **76**, 014312 (2007).

[8] M. Bender, P.-H. Heenen, and P.-G. Reinhard, Rev. Mod. Phys. **75**, 121 (2003).

[9] M. Bender, K. Bennaceur, T. Duguet, P.-H. Heenen, T. Lesinski, and J. Meyer, Phys. Rev. C **80**, 064302 (2009).

[10] P. Sarriguren, R. Rodríguez-Guzmán, and L. M. Robledo, Phys. Rev. C **77**, 064322 (2008).

[11] L. M. Robledo, R. Rodríguez-Guzmán, and P. Sarriguren, J. Phys. G: Nucl. Part Phys. **36**, 115104 (2009).

[12] N. Schunck, J. Dobaczewski, J. McDonnell, J. Moré, W. Nazarewicz, J. Sarich, and M. V. Stoitsov, Phys. Rev. C **81**, 024316 (2010).

[13] K. J. Pototzky, J. Erler, P.-G. Reinhard, and V. O. Nesterenko, Eur. Phys. J. A **46**, 299 (2010).

[14] P. Quentin, L. Bonneau, N. Minkov, and D. Samsœn, Int. J. Mod. Phys. E **19**, 611 (2010).

[15] J. Dobaczewski and J. Dudek, Phys. Rev. C **52**, 1827 (1995); **55**, 3177(E) (1997).

[16] V. Hellemans, P.-H. Heenen, and M. Bender, Phys. Rev. C **85**, 014326 (2012).

[17] L.-G. Cao, G. Colò, H. Sagawa, P. F. Bortignon, and L. Sciacchitano, Phys. Rev. C **80**, 064304 (2009).

[18] C. L. Bai, H. Q. Zhang, X. Z. Zhang, F. R. Xu, H. Sagawa, and G. Colò, Phys. Rev. C **79**, 041301 (2009).

[19] D. Davesne, M. Martini, K. Bennaceur, and J. Meyer, Phys. Rev. C **80**, 024314 (2009); **84**, 059904(E) (2011).

[20] T. Nakatsukasa and K. Yabana, Phys. Rev. C **71**, 024301 (2005).

[21] J. A. Maruhn, P.-G. Reinhard, P. D. Stevenson, and M. R. Strayer, Phys. Rev. C **74**, 027601 (2006).

[22] W. Bothe and W. Gentner, Z. Physik A Hadrons Nucl. **112**, 45 (1939).

[23] G. C. Baldwin and G. S. Klaiber, Phys. Rev. **71**, 3 (1947).

[24] M. Goldhaber and E. Teller, Phys. Rev. **74**, 1046 (1948).

[25] Y. M. Engel, D. M. Brink, K. Goeke, S. J. Krieger, and D. Vautherin, Nucl. Phys. A **249**, 215 (1975).

[26] P. A. M. Dirac, Proc. Camb. Phil. Soc. **26**, 376 (1930).

[27] S. E. Koonin, Ph.D. thesis, Massachusetts Institute of Technology, 1975.

[28] H. Flocard, S. E. Koonin, and M. S. Weiss, Phys. Rev. C **17**, 1682 (1978).

[29] F. Calvayrac, P.-G. Reinhard, and E. Suraud, Ann. Phys. **255**, 125 (1997).

[30] P. D. Stevenson, D. Almehed, P.-G. Reinhard, J. A. Maruhn, J. Rikovska Stone, and M. R. Strayer, *Proceedings of the "Nuclear Structure Physics at the Extremes" Conference, Shimla India* (2005).

[31] C. Simenel and Ph. Chomaz, Phys. Rev. C **68**, 024302 (2003).

[32] S. M. Austin, E. Adamides, A. Galonsky, T. Nees, W. A. Sterrenburg, D. E. Bainum, J. Rapaport, E. Sugarbaker, C. C. Foster, C. D. Goodman, D. J. Horen, C. A. Goulding, and M. B. Greenfield, Phys. Rev. C **63**, 034322 (2001).

[33] F. Osterfeld, Rev. Mod. Phys. **64**, 491 (1992), and references therein.

[34] H. Sagawa and B. Castel, Nucl. Phys. A **435**, 1 (1985).

[35] T. Wakasa, M. Okamoto, M. Takaki, M. Dozono, K. Hatanaka, M. Ichimura, T. Noro, H. Okamura, and Y. Sakemi, Phys. Rev. C **84**, 014614 (2011).

[36] P.-G. Reinhard, P. D. Stevenson, D. Almehed, J. A. Maruhn, and M. R. Strayer, Phys. Rev. E **73**, 036709 (2006).

[37] Ph. Chomaz, N. Van Giai, and S. Stringari, Phys. Lett. B **189**, 375 (1987).

[38] J. M. A. Broomfield and P. D. Stevenson, J. Phys. G: Nucl. Part Phys. **35**, 095102 (2008).

[39] R. Balian and M. Vénéroni, Ann. Phys. **216**, 351 (1992).

[40] D. Lacroix, S. Ayik, and Ph. Chomaz, Prog. Part Nucl. Phys. **52**, 497 (2004), and references therein.

[41] P.-G. Reinhard, Nucl. Phys. A **545**, 59 (1992).

[42] P.-G. Reinhard and E. Suraud, Ann. Phys. **216**, 98 (1992).

[43] J. M. A. Broomfield, Ph.D. thesis, University of Surrey, 2009.

[44] D. Bohm and D. Pines, Phys. Rev. **92**, 609 (1953).

[45] M. Waroquier, J. Ryckebusch, J. Moreau, K. Heyde, N. Blasi, S. Y. van der Werf, and G. Wenes, Phys. Rep. **148**, 249 (1987).

[46] D. Vautherin and D. M. Brink, Phys. Rev. C **5**, 626 (1972).

[47] V. O. Nesterenko, J. Kvasil, and P.-G. Reinhard, Phys. Rev. C **66**, 044307 (2002).

[48] A. M. Lane and J. Martorell, Ann. Phys. **129**, 273 (1980).

[49] G. Colò, P. F. Bortignon, S. Fracasso, and N. Van Giai, Nucl. Phys. A **788**, 173 (2007).

[50] B. Avez, C. Simenel, and Ph. Chomaz, Phys. Rev. C **78**, 044318 (2008).

[51] B. Avez and C. Simenel, arXiv:1105.5217 [nucl-th] (2011).

[52] W. Kohn and L. J. Sham, Phys. Rev. **140**, A1133 (1965).

[53] B. G. Carlsson, J. Dobaczewski, and M. Kortelainen, Phys. Rev. C **78**, 044326 (2008).

[54] D. M. Brink and F. Stancu, Phys. Rev. C **75**, 064311 (2007).

[55] G. Colò, H. Sagawa, S. Fracasso, and P. F. Bortignon, Phys. Lett. B **646**, 227 (2007); **668**, 457(E) (2008).

[56] T. Otsuka, T. Matsuo, and D. Abe, Phys. Rev. Lett. **97**, 162501 (2006).

[57] M. Moreno-Torres, M. Grasso, H. Liang, V. De Donno, M. Anguiano, and N. Van Giai, Phys. Rev. C **81**, 064327 (2010).

[58] E. Perlińska, S. G. Rohoziński, J. Dobaczewski, and W. Nazarewicz, Phys. Rev. C **69**, 014316 (2004).

[59] J. Dobaczewski and J. Dudek, Acta Phys. Pol. B **27**, 45 (1996).

[60] S. Fracasso and G. Colò, Phys. Rev. C **76**, 044307 (2007).

[61] M. Bender, J. Dobaczewski, J. Engel, and W. Nazarewicz, Phys. Rev. C **65**, 054322 (2002).

[62] J. Margueron and H. Sagawa, J. Phys. G: Nucl. Part Phys. **36**, 125102 (2009).

[63] A. Rios, A. Polls, and I. Vidaña, Phys. Rev. C **71**, 055802 (2005).

[64] S. Ebata, T. Nakatsukasa, T. Inakura, K. Yoshida, Y. Hashimoto, and K. Yabana, Phys. Rev. C **82**, 034306 (2010).

[65] I. Stetcu, A. Bulgac, P. Magierski, and K. J. Roche, Phys. Rev. C **84**, 051309(R) (2011).

[66] Y. Haschimoto, Eur. Phys. J. A **48**, 55 (2012).

[67] E. Chabanat, P. Bonche, P. Haensel, J. Meyer, and R. Schaeffer, Nucl. Phys. A **635**, 231 (1998).

[68] W. Zou, G. Colò, Z. Ma, H. Sagawa, and P. F. Bortignon, Phys. Rev. C **77**, 014314 (2008).

[69] E. B. Suckling and P. D. Stevenson, Europhys. Lett. **90**, 12001 (2010).

[70] L.-G. Cao, G. Colò, and H. Sagawa, Phys. Rev. C **81**, 044302 (2010).

[71] T. Duguet, P. Bonche, P.-H. Heenen, and J. Meyer, Phys. Rev. C **65**, 014311 (2001).

[72] S. Fracasso and G. Colò, Phys. Rev. C **72**, 064310 (2005).

[73] P.-G. Reinhard (private communication).

[74] A. S. Umar and V. E. Oberacker, J. Phys. G: Nucl. Part Phys. **36**, 025101 (2009).

[75] J. Erler, P. Klüpfel, and P.-G. Reinhard, J. Phys. G **37**, 064001 (2010).

[76] A. Bohr and B. R. Mottelson, *Nuclear Structure*, Vol. II (Benjamin, Boston, MA, 1975).

[77] A. Migdal, J. Phys. (Moscow) **8**, 331 (1944).

[78] J. O. Newton, B. Herskind, R. M. Diamond, E. L. Dines, J. E. Draper, K. H. Lindenberger, C. Schück, S. Shih, and F. S. Stephens, Phys. Rev. Lett. **46**, 1383 (1981).

[79] V. E. Oberacker, A. S. Umar, J. A. Maruhn, and P.-G. Reinhard, Phys. Rev. C **85**, 034609 (2012).

[80] V. M. Kolomietz, A. G. Magner, and S. Shlomo, Phys. Rev. C **73**, 024312 (2006).

[81] J. J. Gaardhøje, Annu. Rev. Nucl. Part. Sci. **42**, 483 (1992).

[82] H. Steinwedel, J. H. D. Jensen, and P. Jensen, Phys. Rev. **79**, 1019 (1950).

[83] B. L. Berman and S. C. Fultz, Rev. Mod. Phys. **47**, 713 (1975); J. G. Woodworth, K. G. McNeill, J. W. Jury, R. A. Alvarez, B. L. Berman, D. D. Faul, and P. Meyer, Phys. Rev. C **19**, 1667 (1979).

[84] P.-G. Reinhard, Nucl. Phys. A **649**, 305 (1999).

[85] S. Péru and H. Goutte, Phys. Rev. C **77**, 044313 (2008).

[86] J. Bartel, P. Quentin, M. Brack, C. Guet, and H. B. Hånkansson, Nucl. Phys. A **386**, 79 (1982).

[87] C. Losa, A. Pastore, T. Dø ssing, E. Vigezzi, and R. A. Broglia, Phys. Rev. C **81**, 064307 (2010).

[88] Zs. Podolyák, P. H. Regan, M. Pfützner, J. Gerl, M. Hellström *et al.*, Phys. Lett. B **491**, 225 (2000).

[89] R. Kumar, I. M. Govil, A. Dhal, L. Chaturvedi, C. R. Praharaj, A. K. Rath, G. Kiran Kumar, S. K. Basu, A. Chakraborty, Krischichayan, S. Mukhopadhyay, N. S. Pattabiraman, S. S. Ghugre, and A. K. Sinha, Phys. Rev. C **80**, 054319 (2009).

[90] J. A. Maruhn, P. G. Reinhard, P. D. Stevenson, J. R. Stone, and M. R. Strayer, Phys. Rev. C **71**, 064328 (2005).

[91] W. Kleinig, V. O. Nesterenko, J. Kvasil, P.-G. Reinhard, and P. Vesely, Phys. Rev. C **78**, 044313 (2008).

[92] N. Chamel and S. Goriely, Phys. Rev. C **82**, 045804 (2010).

[93] M. Kortelainen and T. Lesinski, J. Phys. G **37**, 064039 (2010).

[94] A. Pastore, K. Bennaceur, D. Davesne, and J. Meyer, Int. J. Mod. Phys. E **21**, 1250040 (2012).

[95] L. Trippa, G. Colò, and E. Vigezzi, Phys. Rev. C **77**, 061304(R) (2008), and references therein.

[96] H. Utsunomiya, P. Mohr, A. Zilges, and M. Rayet, Nucl. Phys. A **777**, 459 (2006).

[97] D. Sarchi, P. F. Bortignon, and G. Colò, Phys. Lett. B **601**, 27 (2004).